ARTICLE

Rapid signalling in distinct dopaminergic axons during locomotion and reward

M. W. Howe[1] & D. A. Dombeck[1]

Dopaminergic projection axons from the midbrain to the striatum are crucial for motor control, as their degeneration in Parkinson disease results in profound movement deficits. Paradoxically, most recording methods report rapid phasic dopamine signalling (∼100-ms bursts) in response to unpredicted rewards, with little evidence for movement-related signalling. The leading model posits that phasic signalling in striatum-targeting dopamine neurons drives reward-based learning, whereas slow variations in firing (tens of seconds to minutes) in these same neurons bias animals towards or away from movement. However, current methods have provided little evidence to support or refute this model. Here, using new optical recording methods, we report the discovery of rapid phasic signalling in striatum-targeting dopaminergic axons that is associated with, and capable of triggering, locomotion in mice. Axons expressing these signals were largely distinct from those that responded to unexpected rewards. These results suggest that dopaminergic neuromodulation can differentially impact motor control and reward learning with sub-second precision, and indicate that both precise signal timing and neuronal subtype are important parameters to consider in the treatment of dopamine-related disorders.

Dopaminergic projections from the substantia nigra pars compacta (SNc) to the striatum are vital for motor control, and their degeneration in neurodegenerative disorders such as Parkinson disease results in severe motor problems[1-3]. However, little evidence for movement-related dopamine signalling has been observed; instead, most recording methods report that unpredicted rewards induce phasic signalling (hundreds-of-millisecond bursts), which are superimposed on slowly varying background activity[4-10]. The leading model to explain the dual role of dopamine in reward and movement posits that phasic bursts in striatum-targeting dopamine neurons act to drive reward-based learning, while slow variations in firing (tens of seconds to minutes) in these same neurons bias the system towards or away from movement[11-15]. However, there is little evidence for or against this model.

Most information about *in vivo* dopamine dynamics comes from extracellular single unit recordings in the ventral tegmental area (VTA) and SNc[6-8,16-21] (Supplementary Discussion). This approach provides functional characterization of individual neurons with single-spike temporal resolution, but it cannot discriminate neurons by their projection targets. Moreover, midbrain single unit recordings alone cannot reliably discriminate dopaminergic from non-dopaminergic neurons[8,22] and are blind to the local control exerted on dopamine terminals in the target regions[23,24]. Fast-scan cyclic voltammetry, on the other hand, measures changes in dopamine release directly in striatal terminal regions, but these measurements of extra-synaptic dopamine, averaged over hundreds of micrometres, are insensitive to synaptically confined dopamine and potentially heterogeneous signalling across different axons[25]. To measure both phasic (hundreds of millisecond) and slowly varying (tens of seconds to minutes) dopamine signalling in the striatum during reward delivery and animal movement, and to determine whether dopamine projections to the striatum broadcast homogenous or heterogeneous signals, we used two-photon calcium imaging and fibre photometry to establish the striatal dopamine signalling patterns occurring in locomoting mice receiving unpredicted rewards. We then tested the role that these activity patterns play in motor control by optogenetically stimulating striatum-targeting dopamine axons.
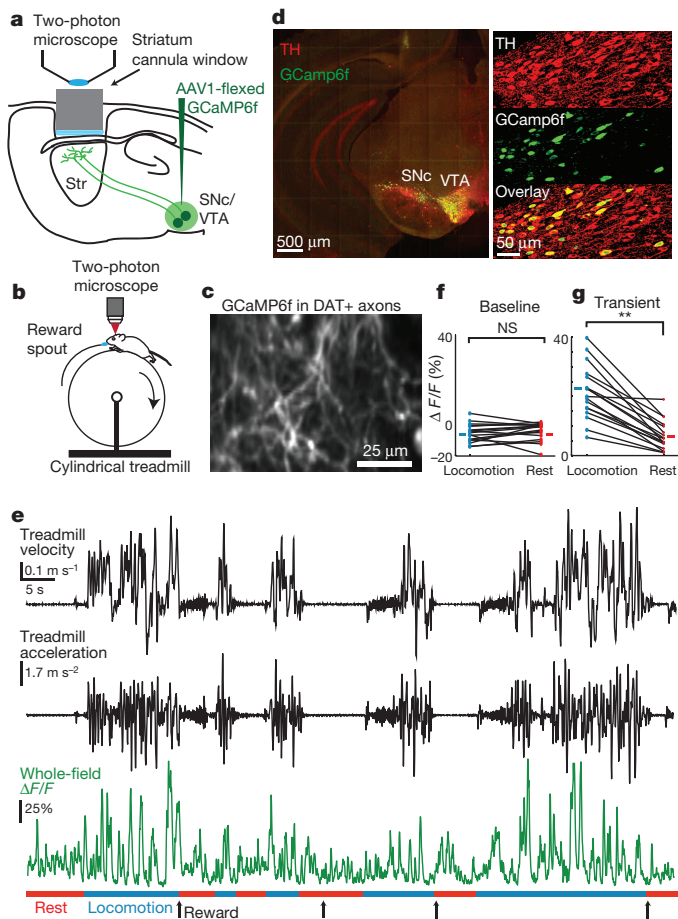
Locomotion related dopamine signalling

A new approach was established to image the activity of dopamine projection axons in dorsal striatum[26] (Fig. 1a–d). DAT-cre mice ($n = 6$) were injected in the midbrain with adenovirus AAV1-Syn-flex-GCaMP6f[27], leading to specific expression of GCaMP6f in dopamine neurons widespread throughout SNc and VTA (Fig. 1d). A chronic imaging window was then implanted over dorsal striatum (Extended Data Fig. 1b) to enable two-photon imaging[26] (Methods, Extended Data Fig. 2i) of the GCaMP6f-expressing dopaminergic projection axons (Fig. 1c). Axons were clearly visible, but were densely packed (Fig. 1c, Extended Data Fig. 1a), presumably representing overlapping axonal arbors from numerous different dopamine neurons[28]. Mice were then head-restrained over a cylindrical treadmill, and time-series videos of the labelled axons were acquired (in the dark) during rest, self-initiated locomotion, and/or delivery of unexpected rewards (Fig. 1e).

Calcium influx into axons and terminals, caused by axonal action potentials[29,30] (with local modulation possible[23,24]), triggers neurotransmitter release[31-33], and therefore, changes in GCaMP6f fluorescence[27] provide an indirect measure of dopamine release in dorsal striatum[34]. These GCaMP6f fluorescence changes are well-suited for determining whether mouse locomotion (100 s of millisecond timescale accelerations) is associated with rapid phasic dopamine signalling (sub-second-duration GCaMP6f transients), slowly varying dopamine signalling (tens of seconds to minutes-duration transients or changes in baseline) or both (Methods, Extended Data Fig. 3a–c).

As a first metric to quantify dopamine signalling in dorsal striatum, we summed the fluorescence from all dopamine axons in each frame of each imaging field (60–250 μm diameter fields sampled at 28 Hz) to generate a mean fluorescence activity trace (mean change in fluorescence, $\Delta F/F$ trace; Fig. 1e, bottom). These traces revealed frequent transients during treadmill locomotion (Fig. 1e), and these varied in duration and amplitude but generally occurred on sub-second timescales (duration 678 ± 460 ms (mean $\pm$ s.d.); amplitude $126 \pm 67\%$ $\Delta F/F$; Extended Data Figs 2g, h, 3e). Longer duration transients often contained multiple peaks, as expected from summation of closely spaced, short duration transients[27] (Fig. 1e, Extended Data Fig. 3).

[1]Department of Neurobiology, Northwestern University, Evanston, Illinois 60208, USA.

Figure 1 | Locomotion related signalling in dorsal-striatal-projecting dopamine axons. a, Schematic of methods. **b**, Mouse running on treadmill under microscope. **c**, Representative field of GCaMP6f-labelled dopamine axons in dorsal striatum. DAT, dopamine transporter. **d**, GCamp6f expression in dopamine neurons (green) overlaid with tyrosine hydroxylase (TH) immunofluorescence (red). Right insets are at high magnification. **e**, Average whole-field $\Delta F/F$ fluorescence from a representative field in one mouse (bottom, $n = 6$ mice total) and corresponding treadmill velocity (top) and acceleration (middle) during locomotion. **f**, Comparison of mean baseline (periods with no significant calcium transients) whole-field $\Delta F/F$ between locomotion and resting periods. **g**, Comparison of mean whole-field fluorescence change (mean of significant calcium transients, excluded baseline periods) between locomotion and resting periods. **f**, **g**, Each point represents mean $\Delta F/F$ for running or resting over one session for each field ($n = 17$ sessions from 6 mice, lines connect same field/session, short lines: mean over sessions); **$P < 10^{-5}$, Wilcoxon rank-sum test. NS, not significant ($P > 0.05$).

Transients were typically synchronous across the densely innervated fields, presumably reflecting widespread co-activation of many projection axons (Extended Data Fig. 1), and were more frequent during spontaneous locomotion than resting (non-reward) periods (Fig. 1g, Extended Data Fig. 4h; $P = 1.8 \times 10^{-4}$, Wilcoxon sign-rank test across all fields, $n = 6$ mice). However, no significant difference in the fluorescence baseline (periods with no significant calcium transients) was found between locomotion and resting (Fig. 1f; $P = 0.45$, Wilcoxon sign-rank test across all fields, $n = 6$ mice). Moreover, the duration of nearly all significant dopamine transients ($n = 2,087$) was far less than the duration of the average locomotion bout (mean locomotion bout 10.3 ± 11.2 s, Extended Data Fig. 3e). Thus in dorsal striatum, treadmill locomotion is associated with widespread and synchronous sub-second transient increases in GCaMP6f fluorescence in dopamine axons, suggestive of phasic dopamine release, but is not associated with detectable long-duration transients or sustained changes in

baseline fluorescence levels, suggesting little slowly-varying dopamine release.

Dopamine signalling to acceleration bursts

We first examined whether the widespread fluorescence transients in dorsal striatum displayed a timing preference with respect to locomotion initiations on the treadmill (sharp rest–run transitions; Fig. 2a, d, f, Extended Data Fig. 4a, b). On average and at individual onsets, GCaMP6f transients increased rapidly just before (~100–150 ms) acceleration onsets occurring at locomotion initiation (Fig. 2a, Extended Data Fig. 4a, j, l, o; cross-correlation peak at -143 ± 250 ms, significantly different from 0 lag, $P = 0.003$, Wilcoxon sign-rank test across peak correlation times, Fig. 2d, f). Thus, signalling across a widespread population of dopaminergic axons leads locomotion initiation in dorsal striatum, suggesting that sub-second dopamine signalling has a role in initiating locomotion bouts.

We then examined whether the widespread fluorescence transients displayed a timing preference with respect to discrete phases of continuous mouse locomotion movements. Movements consisted of rhythmic acceleration bursts on the treadmill over a broad frequency range centred on ~2.5 Hz (Extended Data Fig. 4e).
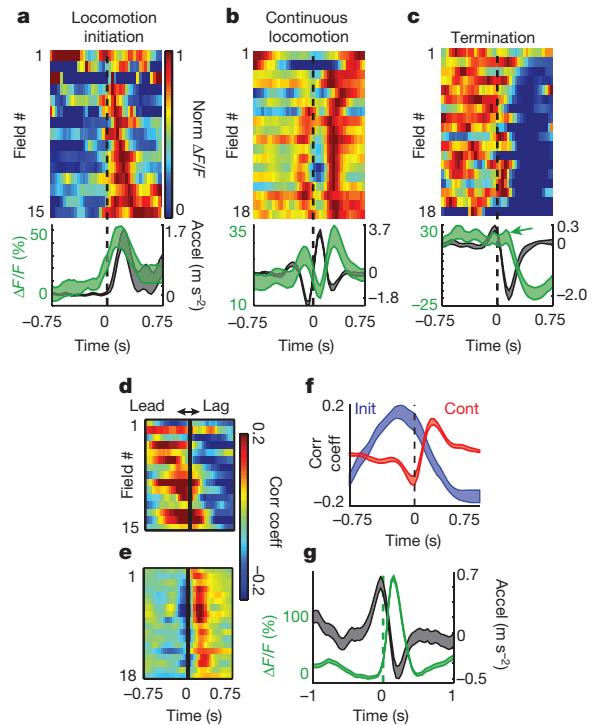

Figure 2 | Phasic dopamine signalling displays a sub-second timing preference with respect to acceleration bursts. a, Top, mean whole-field $\Delta F/F$ triggered on accelerations (accel) at locomotion initiations; each row is mean for each field/session ($\Delta F/F$ normalized for each row and sorted by peak time). Bottom, mean acceleration (black) and whole-field $\Delta F/F$ (green) all triggered on locomotion initiations (mean across all fields). **b**, Same as **a**, except triggered on accelerations during continuous locomotion periods. **c**, Same as **a**, except triggered on locomotion terminations; note lack of $\Delta F/F$ transient peak (arrow) after final acceleration. **d**, Correlations between acceleration and whole-field fluorescence at different relative time-lags (that is, cross-correlations) during locomotion initiation periods (sorted by peak correlation time); each row is mean for each field/session. Corr coeff, correlation coefficient. **e**, Same as **d**, but during continuous locomotion periods. **f**, Mean cross-correlations between acceleration and whole-field fluorescence for initiation (blue) and continuous (red) locomotion periods. **g**, Mean acceleration (black) triggered on all short duration calcium transients (green, mean of transients) during continuous locomotion across all fields. Shaded regions in **a**–**c**, **f**, **g** denotes mean $\pm$ s.e.m.; $n = 6$ mice in **a**–**g**.

Indeed, fluorescence transients displayed a delayed timing preference with respect to acceleration bursts during continuous locomotion (Fig. 2b, e, f, Extended Data Fig. 4c, d), where on average they followed the onsets (zero crossing) of individual acceleration bursts (Fig. 2b,g; cross-correlation peak at 215 ± 90 ms, significantly different from 0 lag, $P = 1.66 \times 10^{-4}$, Wilcoxon sign-rank test across 18 fields; Fig. 2e, f, Extended Data Fig. 5a, b; $n = 6$ mice), an effect that was also clearly observed with individual isolated transients (Extended Data Fig. 4c, k). Importantly, the acceleration-associated calcium transients were observed before the mice ever received rewards on the tread-mill (Extended Data Fig. 4h, i), and the signalling was highly similar after the introduction of unpredicted rewards. Thus, contrary to current widely accepted models, these results establish the existence of a widespread population of dopaminergic axons projecting to the dorsal striatum that display rapid phasic signalling associated with ongoing accelerations, which are expressed independently of reward expectation.

We then investigated whether the dopamine signalling during continuous locomotion might affect subsequent movements. We observed a significant correlation between calcium transient amplitudes and the amplitudes of the immediately following acceleration bursts (Spearman's Rho = 0.13, $P = 0.006$, all transient-acceleration pairs; binned data, Extended Data Fig. 5d), despite a weaker temporal association (compared to previous acceleration bursts, Extended Data Fig. 5a, b). Furthermore, just before locomotion termination (stopping), calcium transient amplitudes associated with the last acceleration burst (before termination) were reduced compared to the transient amplitudes expected from similar acceleration bursts during continuous locomotion (Fig. 2c, arrow). Thus, during continuous locomotion, dopamine axon transients seem to be more temporally associated with the previous (rather than following) acceleration burst (Fig. 2b, e, f, g, Extended Data Fig. 5a, b) and may positively impact the next acceleration burst (Extended Data Fig. 5e), perhaps acting as a feedback signal to promote plasticity or continued locomotion.

Locomotion triggered by dopamine axon stimulation

To test whether sub-second timescale signalling in dopamine axons can trigger or alter locomotion, channelrhodopsin[35] (ChR2) was expressed in midbrain dopamine neurons of DAT-cre mice ($n = 7$) and the dopamine axons in the dorsal striatum were (bi-laterally) optically stimulated (Fig. 3a, Methods). Optical stimulation consisted of 166 or 83 ms duration bursts of 8-ms pulses (pulses repeated at 60 Hz); these bursts were then repeated at 3 or 6 Hz, respectively (see Fig. 3b; frequencies corresponding to rhythmic accelerations measured during average (3 Hz) or fast (6 Hz) locomotion; Extended Data Fig. 4e) to create stimulation trains. This was intended to generate rapid phasic dopamine axon signalling similar to that observed during locomotion. The laser stimulation trains reliably triggered rapid transitions from resting to locomotion (or occasionally rocking forward and back; Fig. 3c–g; statistically significant acceleration increase averaged across all mice and sessions, $P < 0.01$, shuffle test; statistically significant increase in acceleration, averaged across all sessions for 6 out of 7 individual mice, $P < 0.01$, shuffle test), although not every stimulation led to locomotion (Fig. 3d, e). Transitions to locomotion were rapid: for 3 Hz burst trains, acceleration significantly increased from rest after the first burst (that is, ten 8-ms pulses; significantly increased acceleration compared to shuffle ~160 ms after burst onset, $P < 0.01$; Fig. 3g; similar to timing during spontaneous initiations, Fig. 2a, d, f, Extended Data Fig. 4l), whereas for 6 Hz burst trains, acceleration significantly increased from rest after two bursts (that is, two bursts of five 8-ms pulses; significantly increased acceleration compared to shuffle ~240 ms after burst onset, $P < 0.01$; Fig. 3g). Interestingly, 3 or 6 Hz stimulation trains that continued after locomotion initiation were capable of shifting the acceleration frequency in individual mice (Fig. 3h) towards the stimulation frequency during the ensuing locomotion bout. All mice ($n = 7$) displayed higher frequency accelerations during locomotion
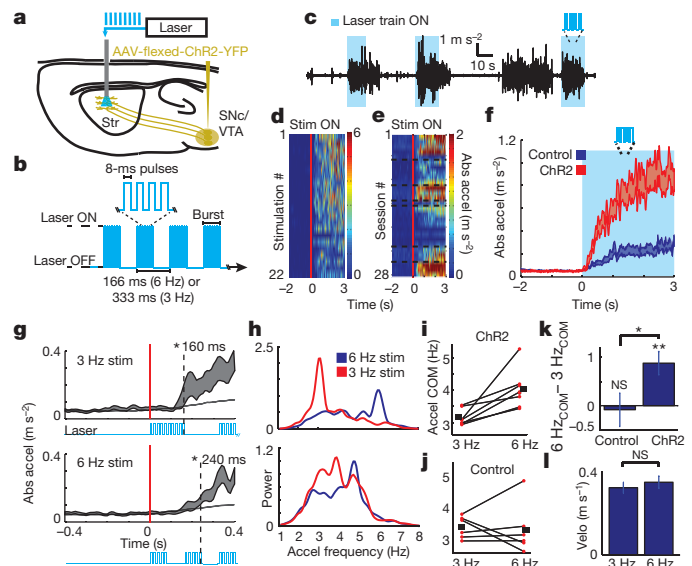
Figure 3 | Pulsed optogenetic stimulation of dorsal-striatum-projecting dopamine axons can rapidly initiate locomotion and control acceleration frequency. a, Schematic of methods. **b**, Pulsed laser delivery protocol for dopamine axon ChR2 stimulation (used for all data presented in this paper). **c**, Representative acceleration from a single stimulation session (blue regions, laser train stimulation to the dorsal striatum). **d**, Absolute value of mouse acceleration aligned on onset of all laser stimulation trains (red line) during a representative single session from one mouse (each row represents a single trial stimulation from rest). **e**, All mean accelerations aligned on laser stimulation trains applied to mice at rest ($n = 7$ mice total, each row represents mean over one session; rows corresponding to sessions for each mouse grouped together; sessions from different mice separated by dashed lines). **f**, Mean absolute (abs) value of mouse accelerations aligned on the onsets of laser stimulation trains applied to mice at rest (mean across all stimulation onsets, $n = 161$ and 267 onsets for ChR2 and control, respectively, in all sessions and mice, 3 and 6 Hz stimulation included). **g**, Same data as **f**, but stimulations separated into 3- or 6-Hz groups and zoomed-in time (blue, laser stimulation). Dashed lines, time when acceleration becomes significantly ($P < 0.01$) greater than random shuffle (thin grey line, mean random shuffle). **h**, Power spectra of acceleration for two representative mice during locomotion periods initiated during 3- and 6-Hz stimulations. **i, j**, Centre of mass of acceleration power spectra (COM) for each ChR2 (**i**) or control (**j**) mouse for locomotion periods initiated during 3-and 6-Hz stimulations. Horizontal bars indicate means, lines connect same mouse. **k**, Mean difference between centre of mass of acceleration power spectra during 3 and 6-Hz stimulations (differences calculated for each mouse) averaged across control or ChR2 mice. **l**, Mean velocity across mice during 3 and 6-Hz stimulations included in **k**. Shaded regions in **f** and **g** denote mean $\pm$ s.e.m. *$P < 0.05$; **$P < 0.01$ (compared to 0), Wilcoxon rank-sum test.

bouts initiated during 6 Hz stimulation than during 3 Hz stimulation (Fig. 3i, k, significant shift, $P < 0.01$, Wilcoxon rank-sum test) despite equivalent mean velocities during these periods (Fig. 3l). In two mice, acceleration power spectra peaks matched the respective stimulation frequencies (one of the two mice in Fig. 3h, top) and accelerations during locomotion were significantly entrained to the laser stimulations ($P < 0.01$, shuffle test; Extended Data Fig. 6a, b; entrainment also significant across all mice, $P < 0.01$ shuffle test, Extended Data Fig. 6c, d). Notably, the same optical stimulation applied to control mice without ChR2 expression failed to trigger locomotion or shift or entrain locomotion frequency ($n = 7$; Fig. 3f, j, k, Extended Data Fig. 6c, d). Thus, optogenetic stimulation of dorsal-striatum-projecting dopamine axons can rapidly trigger locomotion bouts and shift or entrain rhythmic acceleration frequency, demonstrating that signalling in dorsal striatal dopamine axons can impact locomotion movements on sub-second timescales.

Dopamine axon functional heterogeneity

Unpredicted rewards are well-known to trigger phasic bursts of dopamine signalling[6–9,13,18]. Surprisingly, we observed little or no phasic response to randomly delivered water rewards in the mean whole-field $\Delta F/F$ traces; instead the signals decreased in accordance with the deceleration from locomotion to reward consumption or remained flat when reward was delivered at rest (Extended Data Fig. 4f, g). However, a small, sparse population of axons were found that signalled during reward (Fig. 4a). To characterize reward and locomotion signalling at the individual axon level, we then sparsely labelled small populations of midbrain dopamine neurons (Fig. 4b, Extended Data Fig. 7), resulting in sparse labelling of axons in dorsal striatum. This enabled us to resolve the fluorescence changes from putative single axons (Fig. 4c, d, Extended Data Fig. 8a, b) and revealed that, as suggested by the widespread labelling experiments (Fig. 4a), putative single axons in the same dorsal striatum region can differentially signal unpredicted reward and locomotion (Fig. 4d–i). Thus, the dopaminergic projection to the dorsal striatum is heterogeneous with respect to unpredicted reward and locomotion, but is dominated by locomotion signalling.

We then examined whether these functionally distinct axons emanate from different midbrain nuclei[36]. Injections were localized primarily to either SNc ($n = 5$ mice) or medial VTA ($n = 5$ mice) (Extended

Data Fig. 7). In total, 73 isolated putative single axons (Methods) were imaged from SNc and 98 from VTA, of which 63 out of 73 (86%) and 72 out of 98 (73%), respectively, responded to locomotion and/or reward events ($P < 0.01$, Wilcoxon rank-sum test, locomotion versus rest; during unpredicted reward delivery, $P < 0.01$, shuffle test versus non-reward periods; or during both). The large majority of the responsive VTA axons signalled unpredicted reward (Fig. 4k, l, n; 53 out of 72 axons, 74% reward responsive). These responses were consistent with documented single-unit electrophysiology and fast-scan cyclic voltammetry[5,8–10,18,37]: they were absent on omission trials, scaled with reward-size, were not present to licking in the absence of reward, and were present whether reward was delivered during running or rest (Extended Data Fig. 9). In contrast to the VTA, such prominent reward signalling was absent from active dopamine axons emanating from SNc (Fig. 4k, l, n, Extended Data Fig. 9; 0 out of 63 axons). Instead, all event responsive axons from SNc displayed significantly increased signalling during locomotion compared to rest (Fig. 4n; 63 out of 63 axons). This signalling was transient rather than sustained (Fig. 4j, m, Extended Data Fig. 2g, h) and displayed a timing preference with respect to acceleration similar to the whole-field measurements (Fig. 2a–g), indicating that single SNc axons, rather than different subpopulations, can signal during locomotion initiation and continuous locomotion (Extended
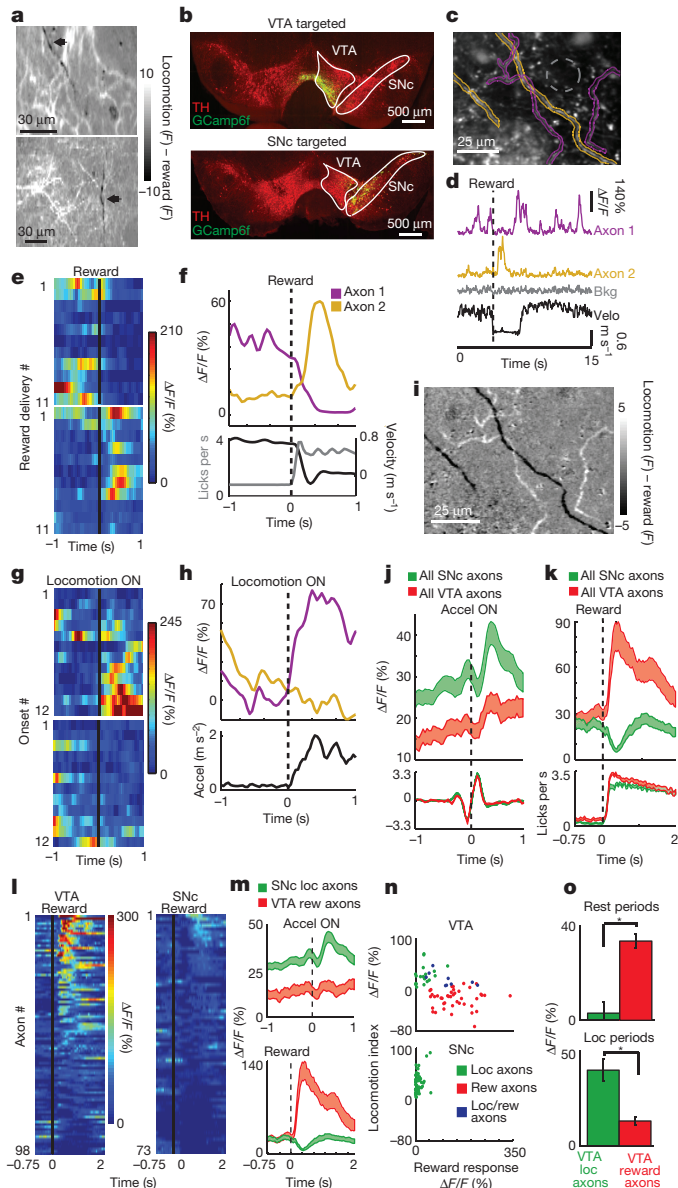
Figure 4 | Functional heterogeneity and anatomical origin of dorsal-striatum-projecting dopamine axons. a, Mean image during locomotion periods minus mean image during reward periods for two representative dopamine axon fields (arrows, axon segments signalling more during reward). **b**, Coronal sections showing restricted GCaMP6f expression (green) in VTA (top) and SNc (bottom) overlaid with tyrosine hydroxylase immunofluorescence (red). **c**, Representative maximum fluorescence projection image from one field in a mouse with GCaMP6f expression localized to VTA ($n = 5$ total VTA-targeted mice). Gold and purple regions are identified regions of interest (ROIs) from putative single axons (grey, background). **d**, $\Delta F/F$ from ROIs in **c** aligned with treadmill velocity and reward time. Bkg, background. **e**, Reward-triggered $\Delta F/F$ from the purple (top) and gold (bottom) ROIs from **c**; each row represents a single reward delivery. **f**, Mean reward-triggered $\Delta F/F$ (gold, purple, top), velocity (black, bottom) and licking (grey, bottom) for the two axons in **c** over the recording session. **g, h**, Same as **e, f**, except triggered on locomotion onsets. **i**, Same as **a**, but for field shown in **c**. **j**, Mean $\Delta F/F$ triggered on acceleration onsets for all putative single axons from all SNc-injected ($n = 5$ mice, 73 axons, green) and VTA-injected ($n = 5$ mice, 98 axons, red) mice. Bottom, mean acceleration. **k**, Mean $\Delta F/F$ triggered on reward for all putative single axons in **j** from SNc (green) and VTA (red). Bottom, mean mouse licking triggered on reward delivery. **l**, Reward-triggered $\Delta F/F$ for all putative VTA (left) and SNc (right) axons (same axons in **j, k**, sorted by reward response magnitude); each row represents mean $\Delta F/F$ for each axon. **m**, Mean $\Delta F/F$ triggered on acceleration onsets (top) and rewards (bottom) for all significant ($P < 0.01$) VTA reward only responsive ($n = 43$ axons from 5 mice, red) and SNc locomotion responsive ($n = 63$ axons from 5 mice, green) axons. **n**, Reward response versus locomotion index for all VTA ($n = 5$ mice, top) and SNc ($n = 5$ mice, bottom) putative axons. Green, significant locomotion; red, significant reward; blue both significant; neither significant not shown. **o**, Mean $\Delta F/F$ during locomotion (bottom) and rest (top, non-reward periods during rest) periods for all locomotion ($n = 19$ axons, 4 mice green) and reward ($n = 43$ axons, 5 mice red) responsive VTA axons. $*P < 10^{-5}$, Wilcoxon rank-sum test. Shaded regions in **j, k** and **m** denote mean ± s.e.m.

Data Fig. 8c–e). Only a minority of the total responsive VTA (Fig. 4k, m–o; 29 out of 72 axons, 40%) and reward signalling VTA (Fig. 4m–o; 10 out of 53 axons, 19%) axons significantly increased signalling during locomotion compared to rest, but similar to the SNc projections, this signalling was transient and acceleration-associated. Overall, reward and locomotion signalling were negatively correlated in the heterogeneous VTA axon population (Fig. 4n; Rho $= -0.51$, $P = 5.7 \times 10^{-6}$). The presence of both reward and locomotion signalling axons from the VTA probably reflects some within-region heterogeneity, however, some expression spillover into SNc[36] or SNc/VTA border region may contribute to the locomotion population. Taken together, these results demonstrate a previously unknown functional heterogeneity within dorsal-striatum-projecting dopamine axons, which, for the most part, arise from different anatomical nuclei: sparsely projecting reward signalling axons originate primarily from VTA while densely projecting SNc originating axons generate an acceleration-associated locomotion-signal.

Dopamine signalling functional topography

Owing to the prominence of unpredicted reward signalling in previous recordings[4,7,9,17,19,37–39], the small fraction of reward signalling dopamine axons in dorsal striatum was surprising. However, because ventral striatum receives most of its dopaminergic innervation from VTA, whereas dorsal striatum receives most from SNc[36], we reasoned that locomotion and unpredicted reward signalling might be similarly graded across the striatum. Single-photon photometry[34,39] was used to record from the GCaMP6f-expressing dopamine axons along the dorsal-ventral axis (Fig. 5a; $n = 5$ mice). This method lacked single axon resolution, but provided a means of recording throughout the striatum with minimal tissue damage. Recordings from dorsal striatum revealed acceleration-associated dopamine signalling highly similar to that observed with two-photon imaging (Figs 1e, 2b versus Fig. 5b–d, Extended Data Fig. 10a–f; serving as a control for the cortical lesion required for two-photon imaging). More ventrally, acceleration-associated signalling declined while unpredicted reward signalling increased (locomotion index versus depth, Rho $= 0.7$, $P = 6 \times 10^{-6}$; reward signal versus depth: Rho $= -0.65$, $P = 5.2 \times 10^{-5}$; Fig. 5c, d, Extended Data Fig. 10g) and dominated in ventral striatum (Fig. 5c, d,

Extended Data Fig. 10g). Consistent with this result, pulsed optogenetic stimulation of dopamine axons in ventral striatum had comparatively little effect on locomotion (Extended Data Fig. 6e–h; $n = 4$ mice, same ChR2-expressing mice as used in Fig. 3). No significant dopamine signalling was seen in the overlying cortex (Fig. 5c, d). Thus, a functional topography in dopamine signalling exists across the striatal dorsal–ventral axis[34], with locomotion and reward signalling dominating dorsal and ventral striatum, respectively.

Discussion

The rapid, phasic, acceleration-associated locomotion signalling of dopamine projection axons described here represent a new mode of dopaminergic modulation of striatal circuitry and establish strong evidence for the long-elusive role for dopamine neurons in fast-timescale motor-control. This result is perhaps surprising given the little evidence for movement-related dopamine signalling previously observed; this difference may be due to task and/or methodological differences (Supplementary Discussion). Our results support new models of dopaminergic signalling that incorporate rapid, sub-second modulation of movement by dopamine[16,20,21] over current models that posit a permissive involvement by a slowly varying background[12,14,15,40] (Extended Data Fig. 10h–k). The phasic signalling occurred in the absence of action requirements or rewards, suggesting a general role in internally driven movement control (Extended Data Fig. 4).

Our optogenetic stimulation experiments support the idea that the phasic signalling in dopamine axons observed with optical recording can trigger and entrain locomotion movements on a sub-second timescale, demonstrating the utility of using measurements of natural neuronal dynamics[41] to define stimulation[35] parameters for effecting a desired behavioural outcome[42]. Dopamine signalling is part of a complex circuit regulating voluntary movement, and therefore is unlikely to instruct movement alone. The behavioural effects of these signals may therefore be strongly modulatory, rather than deterministic, an idea supported by the variability in signalling timing and stimulation effects on locomotion (Fig. 3d, h–k, Extended Data Fig. 4j, k), although this could also be partly owing to the limited region imaged or stimulated. Dopamine signalling could interact differently with the many converging components of the movement network during movement initiations versus continuous movements. At initiations (Fig. 2a, d, f, Extended Data Fig. 4a, b, j), dopamine may provide the necessary motivational drive to execute an intended movement. During ongoing movements, dopamine signalling lagging behind accelerations (Fig. 2b, e, f, g, Extended Data Fig. 4c, d) may modulate upcoming movements (Extended Data Fig. 5d, e), determine whether dorsal striatum circuitry maintains an existing motor pattern (Fig. 2c), or instruct motor learning. Importantly, these findings establish a movement signal that is probably compromised in Parkinson disease, and suggests the potential therapeutic use of restoring precisely timed, movement-associated dorsal striatum dopamine signalling[43].

Finally, distinct populations of axons signalling to reward or locomotion were observed both locally within dorsal striatum and globally across the striatum's dorsal–ventral axis suggesting regional tuning to regulate the specific functions of the terminal regions[34,39]. Heterogeneity of midbrain dopamine neurons has been described in terms of inputs[44,45], gene expression[46–48] and electrophysiological properties[47,49]; such cellular heterogeneity may align with the functional subpopulations described here (Supplementary Discussion)[39,44,45,50]. Specific targeting of these populations, and the local mechanisms such as cholinergic modulation[23,24] that shape their signalling, may provide novel therapeutic opportunities for neurological disorders.
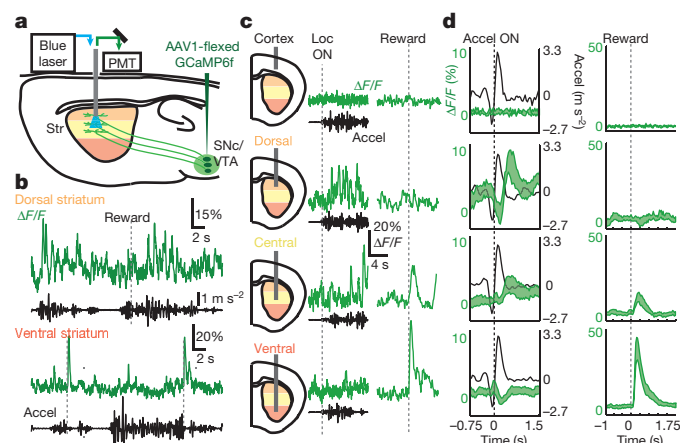
Figure 5 | Functional topography of reward and locomotion dopamine signalling across striatum dorsal-ventral axis. a, Schematic of photometry methods. **b**, Representative photometry $\Delta F/F$ (green) and treadmill accelerations (black) during locomotion and reward delivery (dashed lines) periods from dorsal (top) and ventral (bottom) striatum from same mouse (same session, $n = 5$ mice total). **c**, Representative photometry $\Delta F/F$ from individual locomotion initiations (left) and reward deliveries (right) measured at indicated depths (not averaged). **d**, Mean $\Delta F/F$ across all photometry recording sessions ($n = 5$ mice) triggered on acceleration onsets (left) and reward deliveries (right) at depths indicated in **c** (black, mean acceleration).

1. Dauer, W. & Przedborski, S. Parkinson's disease: mechanisms and models. *Neuron* **39,** 889–909 (2003).
2. Hornykiewicz, O. [Dopamine (3-hydroxytyramine) in the central nervous system and its relation to the Parkinson syndrome in man]. *Dtsch. Med. Wochenschr.* **87,** 1807–1810 (1962).
3. Carlsson, A. Evidence for a role of dopamine in extrapyramidal functions. *Acta Neuroveg. (Wien)* **26,** 484–493 (1964).
4. Day, J. J., Roitman, M. F., Wightman, R. M. & Carelli, R. M. Associative learning mediates dynamic shifts in dopamine signaling in the nucleus accumbens. *Nat. Neurosci.* **10,** 1020–1028 (2007).
5. Howe, M. W., Tierney, P. L., Sandberg, S. G., Phillips, P. E. & Graybiel, A. M. Prolonged dopamine signalling in striatum signals proximity and value of distant rewards. *Nature* **500,** 575–579 (2013).
6. Romo, R. & Schultz, W. Dopamine neurons of the monkey midbrain: contingencies of responses to active touch during self-initiated arm movements. *J. Neurophysiol.* **63,** 592–606 (1990).
7. Pan, W. X., Schmidt, R., Wickens, J. R. & Hyland, B. I. Dopamine cells respond to predicted events during classical conditioning: evidence for eligibility traces in the reward-learning network. *J. Neurosci.* **25,** 6235–6242 (2005).
8. Cohen, J. Y., Haesler, S., Vong, L., Lowell, B. B. & Uchida, N. Neuron-type-specific signals for reward and punishment in the ventral tegmental area. *Nature* **482,** 85–88 (2012).
9. Mirenowicz, J. & Schultz, W. Importance of unpredictability for reward responses in primate dopamine neurons. *J. Neurophysiol.* **72,** 1024–1027 (1994).
10. Hamid, A. A. *et al.* Mesolimbic dopamine signals the value of work. *Nat. Neurosci.* **19,** 117–126 (2016).
11. Berridge, K. C. The debate over dopamine's role in reward: the case for incentive salience. *Psychopharmacology (Berl.)* **191,** 391–431 (2007).
12. Schultz, W. Multiple dopamine functions at different time courses. *Annu. Rev. Neurosci.* **30,** 259–288 (2007).
13. Schultz, W., Dayan, P. & Montague, P. R. A neural substrate of prediction and reward. *Science* **275,** 1593–1599 (1997).
14. Mazzoni, P., Hristova, A. & Krakauer, J. W. Why don't we move faster? Parkinson's disease, movement vigor, and implicit motivation. *J. Neurosci.* **27,** 7105–7116 (2007).
15. Niv, Y., Daw, N. D., Joel, D. & Dayan, P. Tonic dopamine: opportunity costs and the control of response vigor. *Psychopharmacology (Berl.)* **191,** 507–520 (2007).
16. Jin, X. & Costa, R. M. Start/stop signals emerge in nigrostriatal circuits during sequence learning. *Nature* **466,** 457–462 (2010).
17. Puryear, C. B., Kim, M. J. & Mizumori, S. J. Conjunctive encoding of movement and reward by ventral tegmental area neurons in the freely navigating rodent. *Behav. Neurosci.* **124,** 234–247 (2010).
18. Tobler, P. N., Fiorillo, C. D. & Schultz, W. Adaptive coding of reward value by dopamine neurons. *Science* **307,** 1642–1645 (2005).
19. Roesch, M. R., Calu, D. J. & Schoenbaum, G. Dopamine neurons encode the better option in rats deciding between differently delayed or sized rewards. *Nat. Neurosci.* **10,** 1615–1624 (2007).
20. Barter, J. W. *et al.* Beyond reward prediction errors: the role of dopamine in movement kinematics. *Front. Integr. Neurosci.* **9,** 39 (2015).
21. Dodson, P. D. *et al.* Representation of spontaneous movement by dopaminergic neurons is cell-type selective and disrupted in parkinsonism. *Proc. Natl Acad. Sci. USA,* **113,** E2180–E2188 (2016).
22. Margolis, E. B., Lock, H., Hjelmstad, G. O. & Fields, H. L. The ventral tegmental area revisited: is there an electrophysiological marker for dopaminergic neurons? *J. Physiol. (Lond.)* **577,** 907–924 (2006).
23. Wang, L. *et al.* Modulation of dopamine release in the striatum by physiologically relevant levels of nicotine. *Nat. Commun.* **5,** 3925 (2014).
24. Threlfell, S. *et al.* Striatal dopamine release is triggered by synchronized activity in cholinergic interneurons. *Neuron* **75,** 58–64 (2012).
25. Robinson, D. L., Venton, B. J., Heien, M. L. & Wightman, R. M. Detecting subsecond dopamine release with fast-scan cyclic voltammetry *in vivo*. *Clin. Chem.* **49,** 1763–1773 (2003).
26. Dombeck, D. A., Harvey, C. D., Tian, L., Looger, L. L. & Tank, D. W. Functional imaging of hippocampal place cells at cellular resolution during virtual navigation. *Nat. Neurosci.* **13,** 1433–1440 (2010).
27. Chen, T. W. *et al.* Ultrasensitive fluorescent proteins for imaging neuronal activity. *Nature* **499,** 295–300 (2013).
28. Matsuda, W. *et al.* Single nigrostriatal dopaminergic neurons form widely spread and highly dense axonal arborizations in the neostriatum. *J. Neurosci.* **29,** 444–453 (2009).
29. Petreanu, L. *et al.* Activity in motor-sensory projections reveals distributed coding in somatosensation. *Nature* **489,** 299–303 (2012).
30. Cox, C. L., Denk, W., Tank, D. W. & Svoboda, K. Action potentials reliably invade axonal arbors of rat neocortical neurons. *Proc. Natl Acad. Sci. USA* **97,** 9724–9728 (2000).
31. Turner, T. J. Nicotine enhancement of dopamine release by a calcium-dependent increase in the size of the readily releasable pool of synaptic vesicles. *J. Neurosci.* **24,** 11328–11336 (2004).
32. Woodward, J. J., Chandler, L. J. & Leslie, S. W. Calcium-dependent and -independent release of endogenous dopamine from rat striatal synaptosomes. *Brain Res.* **473,** 91–98 (1988).
33. Tritsch, N. X., Ding, J. B. & Sabatini, B. L. Dopaminergic neurons inhibit striatal output through non-canonical release of GABA. *Nature* **490,** 262–266 (2012).
34. Parker, N. F. *et al.* Reward and choice encoding in terminals of midbrain dopamine neurons depends on striatal target. *Nat. Neurosci.* **19,** 845–854 (2016).
35. Boyden, E. S., Zhang, F., Bamberg, E., Nagel, G. & Deisseroth, K. Millisecond-timescale, genetically targeted optical control of neural activity. *Nat. Neurosci.* **8,** 1263–1268 (2005).
36. Ikemoto, S. Dopamine reward circuitry: two projection systems from the ventral midbrain to the nucleus accumbens-olfactory tubercle complex. *Brain Res. Rev.* **56,** 27–78 (2007).
37. Hollerman, J. R. & Schultz, W. Dopamine neurons report an error in the temporal prediction of reward during learning. *Nat. Neurosci.* **1,** 304–309 (1998).
38. Schultz, W. & Romo, R. Dopamine neurons of the monkey midbrain: contingencies of responses to stimuli eliciting immediate behavioral reactions. *J. Neurophysiol.* **63,** 607–624 (1990).
39. Lerner, T. N. *et al.* Intact-brain analyses reveal distinct information carried by SNc dopamine subcircuits. *Cell* **162,** 635–647 (2015).
40. Salamone, J. D. & Correa, M. The mysterious motivational functions of mesolimbic dopamine. *Neuron* **76,** 470–485 (2012).
41. Dombeck, D. A., Khabbaz, A. N., Collman, F., Adelman, T. L. & Tank, D. W. Imaging large-scale neural activity with cellular resolution in awake, mobile mice. *Neuron* **56,** 43–57 (2007).
42. Steinberg, E. E. & Janak, P. H. Establishing causality for dopamine in neural function and behavior with optogenetics. *Brain Res.* **1511,** 46–64 (2013).
43. Steinberg, J. A. *et al.* Optogenetics enables functional analysis of human embryonic stem cell-derived grafts in a Parkinson's disease model. *Nat. Biotechnol.* **33,** 204–209 (2015).
44. Lammel, S. *et al.* Input-specific control of reward and aversion in the ventral tegmental area. *Nature* **491,** 212–217 (2012).
45. Beier, K. T. *et al.* Circuit architecture of VTA dopamine neurons revealed by systematic input-output mapping. *Cell* **162,** 622–634 (2015).
46. Poulin, J. F. *et al.* Defining midbrain dopaminergic neuron diversity by single-cell gene expression profiling. *Cell Rep.* **9,** 930–943 (2014).
47. Roeper, J. Dissecting the diversity of midbrain dopamine neurons. *Trends Neurosci.* **36,** 336–342 (2013).
48. Lammel, S. *et al.* Diversity of transgenic mouse models for selective targeting of midbrain dopamine neurons. *Neuron* **85,** 429–438 (2015).
49. Matsumoto, M. & Hikosaka, O. Two types of dopamine neuron distinctly convey positive and negative motivational signals. *Nature* **459,** 837–841 (2009).
50. Gunaydin, L. A. *et al.* Natural neural projection dynamics underlying social behavior. *Cell* **157,** 1535–1551 (2014).

Supplementary Information is available in the online version of the paper.

Author Contributions M.W.H. performed the experiments, D.A.D. built the experimental apparatus, M.W.H. performed data analysis with strategy suggestions from D.A.D. Both authors conceived and designed the experiments, interpreted the data and wrote the paper.

METHODS

Virus injections for optical recording. All experiments were approved by the Northwestern University Animal Care and Use Committee. Heterozygous adult male mice (postnatal 3–4 months) with Cre expression in DAT-containing midbrain dopamine neurons (GENSAT line Tg(Slc6a3-cre)SG62Gsat/Mmucd) were anaesthetized with isofluorane (1–2%). For achieving widespread expression of GCaMP6f in dopaminergic neurons ($n = 6$, Figs 1, 2, 4a, 5, Extended Data Figs 1, 2k, 3e, 4, 5, 10), a 0.5–1-mm diameter craniotomy was made over the right midbrain (−3.4 mm caudal, +1.0 lateral from bregma). A small volume (0.04 μl) of flexed-GCaMP6f virus (AAV1-Syn-flex-GCaMP6f, 1.4×10^{13} genome copies (GC) ml^{-1} diluted 1:1 in PBS; University of Pennsylvania vector core) was pressure injected through a pulled glass micropipette into the midbrain at two caudal locations (∼−3.3 and −3.5 mm from bregma) and 3 depths at each location (−4.1, −4.4 and −4.7 mm ventral from dura surface) for a total volume of ∼0.24 μl. For sparse, targeted injections (Fig. 4b–o, Extended Data Figs 2, 3, 7–9), the craniotomy was centred over either the medial VTA ($n = 5$; caudal −3.1 mm, lateral 0.2 mm) or lateral SNc ($n = 5$; caudal −3.4 mm, lateral 1.5 mm) and virus (0.025–0.05 μl) was injected at two ventral locations (−4.3, −4.6 mm) for a total of ∼0.08 μl. Following the injections, the skull and craniotomy were sealed with Metabond (Parkell) and a custom metal headplate.

Dorsal striatum window implant surgery. One week after injection, mice were again anaesthetized, and the headplate and metabond removed. A ∼2.75 mm craniotomy was performed above the dorsal striatum (+0.5 mm rostral, +1.8–2.1 mm lateral to bregma) and cortical tissue was aspirated until the internal capsule fibres overlying the striatum were exposed[26]. Some of these fibres were then carefully removed until only a thin layer remained over the striatal surface. A thin (∼100 μm) layer of Kwik-Sil (WPI) was applied over the imaging region, and a metal cannula (stainless-steel tube, 2.7 mm outer diameter, 2.3 mm inner diameter, 1.6 mm length) covered at one end by a glass coverslip[26] was inserted into the aspiration site down to the fibre surface (Extended Data Fig. 2i). The imaging cannula, along with a metal headplate, and positioning ring (see ref. 26 for details) were sealed and attached to the skull with Metabond.

Behaviour and two-photon imaging. After the window surgery, the mice were allowed to recover in their home cages for ∼2–3 days. After this time, the mice began water scheduling (receiving ∼0.8–1 ml of water per day) as described previously[26,51]. The mice displayed no obvious signs of motor deficits following window implantation or water scheduling. Then 3–4 weeks after implant surgery, mice were head-fixed with their limbs resting on a 1D cylindrical styrofoam treadmill ∼20 cm in diameter by 13 cm wide (treadmill described previously[52], Fig. 1b) in the dark, which allowed them to run freely forwards and backwards. Large (16 μl) and small volume (4 μl) water rewards were delivered at pseudo-random time intervals (28.1 ± 19.8 s; mean ± s.d.) through a water spout gated electronically through a solenoid valve once imaging began, and spout licking was measured by a contact monitoring circuit. Solenoid valve triggering was accompanied by a short 'click' noise, which allowed us to conduct reward omission trials in which the water tube was manually closed (Extended Data Fig. 9a, b). Rotational velocity of the treadmill during locomotion was sampled at 1,000 Hz by a rotary encoder (E2-5000, US Digital used for most experiments; a few early experiments used a E6B2-CWZ3E, Yumo) attached to the axel of the treadmill. Instantaneous acceleration was calculated as the difference between consecutive treadmill velocity (first smoothed over two bins) measurements. Live video of behaviour on the treadmill was recorded at 30 Hz via a table mounted infared CCD camera (Computa) illuminated by an infared light source.

Two-photon imaging was performed using a custom, table mounted microscope system and data acquisition system described in ref. 53 (except the electric lens was not used here). Laser (920 nm) average power was in the range of 100–200 mW, but typically closer to 100 mW. This power measurement was made after the objective (Olympus LUMPlanFL N, 40×, 0.8 NA), but before the cannula, which apertures the excitation light, likely further reducing the power reaching the striatum. A Digidata1440A (Molecular Devices) data acquisition system was used to record (Clampex 10.3) and synchronize reward timing, licking, wheel velocity, and two-photon image frame timing. Imaging sessions began after mice were acclimated to head fixation and ran frequently on the treadmill (∼1–3 days). To rule out the influence of prior reward experience on locomotion responses, a subset of mice ($n = 4$) were imaged before receiving any water rewards on the wheel (Extended Data Fig. 4h, i). Time-series videos (3,000–12,000 frames) were acquired at 28 Hz (256 × 64 pixels, 0.5 ms per line). A subset of the sparsely labelled single axon recordings were performed at 14 Hz (256 × 128 pixels, 0.5 ms per line) to achieve better spatial resolution for resolving small axonal arbors. For triggered averages (Fig. 4j, k, m), $\Delta F/F$ fluorescence traces generated from these 14 Hz imaging data sets were linearly interpolated to match the data collected at the 28 Hz sampling rates. Field of view sizes ranged from ∼60 to 250 μm.

Striatum imaging fields (60–250 μm diameter fields) were selected based on the presence of fibre morphology with at least occasional calcium transients in the fibres (field were not selected based on the behavioural correlation of the transients, only whether transients were clearly present) and, for widespread dopamine neuron expression experiments (Figs 1, 2, Extended Data Figs 1, 3, 4, 5), densely labelled projections across the field, or for sparse dopamine neuron expression experiments (Fig. 4, Extended Data Figs 7–9), few labelled projections in the field. Fields ranged in depth from 20–100 μm below the fibre surface. Each mouse was imaged for ∼5–10 days, with multiple fields imaged per day (an 'imaging session' consisted of time-series recording from a single field, typically for many minutes); ∼5–15 total different fields were imaged per mouse across all days (not all sessions met behaviour criteria to be included in all analyses, see below); no attempt was made to locate the same imaging field/axons from day to day, except in a small subset of experiments to demonstrate that axon morphology and behavioural signalling remains stable over days (Extended Data Fig. 2). Imaging up to ∼700 μm from the centre of the cannula was possible, although most fields were acquired near the centre of the cannula. Thus, most of our imaging fields were located more laterally in the dorsal striatum (∼1.5–2.4 mm lateral from the midline), but some medial fields were obtained as well (most medial, ∼1.1 mm from midline, Extended Data Fig. 1). Imaging along the rostral–caudal axis ranged from −0.2 to 1.2 mm from bregma. There was no preference for recording location within this large range of positions and no obvious differences in dopamine signalling were observed within this range.

Interpretation of mechanisms underlying calcium transients and characterization of putative single dopamine axon calcium transients. The time course of fluorescence changes caused by changes in cytoplasmic calcium concentration are well-known and characterized[27,30], providing a significant framework within which to interpret our observed calcium transients (Extended Data Fig. 3a–c). For example, a short tens of milliseconds timescale influx of calcium (such as a short burst of action potentials over tens of milliseconds) results in a stereotyped calcium transient consisting of a fluorescence increase to peak over ∼50–70 ms followed by an exponential decay to baseline over ∼150–250 ms (Extended Data Fig. 3a). Multiple influx events separated by less than the indicator decay time (for example, longer bursts of action potential firing over ∼100s of milliseconds) lead to longer duration, larger amplitude calcium transients due to summation (Extended Data Fig. 3b), while a sustained increase in the rate of influx events separated by less than the decay time (for example, sustained increase in action potential firing) leads to sustained elevations or apparent shifts in the fluorescence baseline due to ongoing summation[54] (Extended Data Fig. 3c, left). Thus, GCaMP6f fluorescence changes are well-suited for determining whether mouse locomotion (accelerations on the 100s of millisecond timescale) is associated with sub-second phasic dopamine signalling (rapid transient changes in fluorescence), slowly varying dopamine signalling (long-duration transients or changes in the GCaMP6f baseline level over many seconds or minutes) or both. However, our imaging methods probably cannot reliably detect single action potentials in single axons, or the difference in transient amplitude due to an additional spike in a burst. Furthermore, it is possible that small, slow changes in action potential firing could occur between rest and locomotion and not be detected using our optical recording methods. Also, although we did not detect slow changes in signalling here, such changes could occur over timescales longer than our typical recording sessions (many minutes).

Optical stimulation of dopamine axons. To achieve widespread expression of ChR2 in dopaminergic axons in the striatum, DAT-cre mice ($n = 7$; 5 male, 2 female; postnatal 3–6 months) were injected bilaterally (0.2–0.3 μl total per hemisphere) as above with AAV9-EF1a-DIO-hChR2 (University of Pennsylvania vector core diluted 3:1 in PBS to 3.5×10^{12} GC ml^{-1}) in the midbrain (−3.3 mm caudal, ±1.3 mm lateral from bregma) at three depths (−4.1, −4.4, −4.7 mm from the dura surface). Headplates for head fixation were then attached to the skull with a thin layer of Metabond and the location of the striatum (+0.5 mm rostral, ±1.8 mm lateral from bregma) was marked on the surface. After 4–6 weeks[55], mice were anaesthetized with isofluorane and small craniotomies (∼0.5–1 mm in diameter) were drilled (at the pre-marked locations) through the Metabond and skull over the striatum, leaving the dura and cortex intact. The craniotomy was then sealed with Kwik-Sil. After the mice recovered from this short (∼10–15 min) surgery for at least one day, they were head-fixed on the linear treadmill. When mice began to exhibit periodic, spontaneous run-rest transitions on the treadmill, the Kwik-Sil covering the craniotomies was removed and two optical fibres (200 μm diameter, ThorLabs) were lowered slowly into the brain bilaterally (to various depths ranging from dorsal (1.6–2.2 mm) to ventral (3.6–4.1 mm) striatum) to allow for delivery of laser light (488 nm diode laser, Thor Labs). Laser stimulation (5 mW laser power at the fibre tip) trains consisted of 83 ms ON/83 ms OFF (6 Hz) or 166 ms ON/166 ms OFF (3 Hz) periods and the laser was pulsed (8 ms ON/8 ms OFF, using an optical chopper, ThorLabs) during the 83 or 166 ms ON periods.

We refer to this stimulation as a train of 8-ms pulse bursts repeated at 3 or 6 Hz. For example, for 6-Hz stimulation, the laser stimulation trains consisted of the following: 8 ms ON/8 ms OFF/8 ms ON/8 ms OFF (repeated for 83 ms) followed by 83 ms with no stimulation and then the whole sequence repeated (Fig. 3b). The onset of laser stimulation trains were triggered manually via a pulse generator and synchronized to output from the treadmill rotary encoder through our data acquisition system (see above). Stimulation trains (duration 8.6 ± 2.8 s) were initiated periodically at pseudo-random intervals primarily during rest periods during 1–8 stimulation blocks (sessions) per mouse per day at varying depths in the striatum (3–5 min block durations, all occurring during a single ~40 min recording period on the treadmill per day per mouse). Importantly, bright LED lights (470 nM and 530 nM ThorLabs) provided constant illumination onto the face of the mice on the treadmill during the stimulation blocks to mask the mice from the fibre optic light delivered to their brain. After stimulation was completed, craniotomies were again covered with Kwik-Sil to allow for additional sessions on subsequent days (1–3 days per mouse). We note that effects highly similar to those shown in Fig. 3 and Extended Data Fig. 6a–d were obtained using the above laser stimulation trains, but with either faster pulsing (4 ms ON/4 ms OFF) during the 83 or 166 ms ON periods or no pulsing at all (only 83 ms ON/83 ms OFF, 6 Hz or 166 ms ON/166 ms OFF, 3 Hz); however all data presented in the manuscript were obtained using the 8-ms pulsing during bursts protocol.

Single fibre photometry. For fibre photometry, we coupled the blue diode laser excitation light (488 nm diode laser, Thor Labs; filtered using a 488/6 nm filter, Semrock) into an optical fibre (200 μm diameter, ThorLabs) and used neutral density filters between the laser and fibre coupling lens to adjust power (1 mW at fibre tip). Fluorescence was collected through the same fibre and was separated from the excitation light by placing a dichroic mirror (505 nm-shortpass, Semrock) between the laser and fibre coupling lens. Fluorescence light was further filtered (540/50 nm, Semrock) and then measured using a GaAsP PMT (H10770PA-40, Hamamatsu). The PMT signal was digitized and recorded using the electronics and ScanImage software from our two-photon microscope (described above). Synchronization of the recorded fluorescence with treadmill movements was accomplished as described above for two-photon imaging.

DAT-cre mice ($n = 5$) were injected with viral vectors to obtain ubiquitous GCaMP6f expression in midbrain dopamine neurons as described above for two-photon imaging experiments and fitted with plates for head-fixation as described for the ChR2 experiments. At 3–5 weeks after injection, mice were trained for 1–3 days on the linear treadmill with rewards until they ran reliably. Mice were then anaesthetized with isoflourane and a unilateral craniotomy (~0.5–1 mm in diameter, dura and cortex were left intact) over the central striatum (+0.5 A/P, +1.3–1.8 mm M/L from bregma) was performed. After recovery from the short (~10–15 min) surgery, mice were head-fixed on the linear treadmill. When mice began to run regularly on the treadmill, the optical fibre was lowered slowly into the brain to various depths ranging from Cortex to Ventral Striatum for photometry recording (Fig. 5, Extended Data Fig. 10). Unpredicted rewards were delivered as described above.

Data analysis. Data were analysed using ImageJ (1.46) and custom functions written in MATLAB (Version 2012b). Sample sizes were chosen to reliably measure experimental parameters while remaining in compliance with ethical guidelines to minimize the number of animals used. Experiments did not involve blinding, but randomization was used with respect to reward delivery and order of data collection from control versus experimental mice. All data in the text and figures are labelled as either mean ± s.d. or mean ± s.e.m.

Motion correction and ROI selection for two-photon microscopy. Each time-series video was motion corrected using algorithms described previously[26,56]. Videos were then visibly inspected to confirm post-correction image stability and videos with excessive motion artefact or apparent z-shifts were excluded from analysis. To quantify whole-field fluorescence (Figs 1, 2, Extended Data Figs 1, 2k, 3e, 4, 5) a single large region of interest (ROI) was hand-selected (to contain all the active regions of the field) from the mean fluorescence image for each time series. Fluorescence traces and ROIs from putative single axon segments from the sparsely labelled fields (Fig. 4, Extended Data Figs 7–9) were generated using CellSort[57] with the following parameters: smoothing width = 1.5, mu = 0.8, principal components = 200, area limits = 50–3,000 pixels. ROI fluorescence traces and ROI morphology were visibly inspected and selected for inclusion as a putative axon if they exhibited elongated morphology consistent with axons (Fig. 4c) and activity patterns with predominantly positive-going fluorescence changes (no structures with slowly varying fluorescence activity patterns were observed). The fluorescence traces were then baseline normalized (eighth percentile fluorescence over a 1,000 bin, ~35.7 s, sliding window, to remove any slow drifts in baseline; see below for measurements of slow changes in baseline) and converted to $\Delta F/F$. Significant positive-going transients (used for Figs 1g, 2g, 4k–o; Extended Data

Figs 2g, h, 3d, e, 4h, i (bottom), 5a, b, 7–9, 10a–c) were identified as previously described[26]. To account for axon segments that probably originated from the same neuron, hierarchical clustering (simple linkage) of the linear correlation matrix between $\Delta F/F$ traces of all segments in each field was performed using a correlation coefficient threshold of 0.8 (results were similar using other clustering thresholds, Extended Data Fig. 8a, b), and $\Delta F/F$ traces belonging to the same cluster were averaged. To verify single axon separation from background, analysis was repeated only on the most sparsely expressing fields; separation of functional axon classes was qualitatively similar to Fig. 4n using this more conservative approach (data not shown).

Relationship of fluorescence signals to treadmill locomotion. All mice ($n = 6$ whole field, $n = 5$ for each single-axon imaging group, $n = 5$ for photometry) contributed to averaged measures unless otherwise noted in the text or figure captions. Individual imaging sessions were excluded if they did not meet criteria for each specific behavioural analysis (that is, locomotion initiation, continuous locomotion, locomotion terminations; see below for each), hence the session numbers varied slightly for each measure. For general comparisons of fluorescence changes in whole fields and single axons during locomotion and rest periods (Figs 1f, g, 4n, o, Extended Data Figs 2f, 4h, 7, 8,10a–c, g), we classified each imaging frame (~35-ms bin size) as occurring during active locomotion, passive rest, or neither (uncertain, excluded). All bins occurring within 5.5 s post-reward delivery or during a spontaneous licking period were excluded. Locomotion bins were identified as those that had a treadmill velocity measure greater than 0.2 m s^{-1} and an acceleration greater than 1.7 m s^{-2} in a 200-ms window on either side. Conversely, rest bins were defined as having no accelerations greater than 0.3 m s^{-2} or velocities greater than 0.05 m s^{-1}. These parameters were determined based upon visual comparison of live video with acceleration and velocity traces and are probably conservative constraints. To be included for locomotion/rest comparisons, behaviour over the entire imaging session had to include a minimum of 30 rest bins and 30 locomotion bins. Slow, sustained changes in baseline fluorescence (Figs 1f and Extended Data Fig. 10a–c) were quantified by comparing $\Delta F/F$ for locomotion and resting periods that did not contain significant calcium transients. The $\Delta F/F$ baseline normalization was re-computed for this calculation using a larger sliding window (2,000 bins, ~70.4 s) to ensure that slow events over multiple locomotion bouts (Extended Data Fig. 3e) would be detected if they were present. Further, examination of $\Delta F/F$ traces with no baseline normalization did not reveal slow events corresponding to locomotion bouts (Extended Data Fig. 2k).

Locomotion initiation times for triggered averages of fluorescence (Figs 2a, d, f, 4h, Extended Data Figs 4a, b, j, 10d–f) were first identified manually by visual inspection of velocity traces for each session. Typically, mice exhibited clear transitions between rest (periods with few treadmill accelerations) and continuous treadmill locomotion. Bursts of acceleration not followed by a prolonged elevation in velocity (indicative of continuous locomotion) were not selected. Manually selected initiations were included for analyses only if they were followed (within 10 bins, ~350 ms) by an acceleration peak greater than 1 m s^{-2} and were not preceded within 1 s by any velocity bins larger than 0.05 m s^{-1} or accelerations larger than 0.3 m s^{-2}. Acceleration-triggered averages were calculated relative to the onset of the first acceleration (after the manually defined time point) greater than 0.3 m s^{-2}. Locomotion terminations (Fig. 2c) were also selected manually as the first deceleration to rest following locomotion bouts. One termination time-point was selected for each initiation. Terminations were included if they were preceded (within 10 bins) by a maximum velocity greater than 0.1 m s^{-1}, indicating a sharp locomotion to rest transition. For defining periods of acceleration occurring during continuous running (Fig. 2b, e, f, Extended Data Figs 4c, d, k, m, 8d, e), accelerations were required to be preceded (within a ~200-ms window) by a minimum run velocity of (0.1 m s^{-1}) and followed by a mean run velocity (over 200 ms) of 0.1 m s^{-1}. Non behaviour-specific acceleration triggered averages of fluorescence (Figs 4j, m, 5d, Extended Data Fig. 4i, top) were calculated for all accelerations exceeding 1.7 m s^{-2} (that is, accelerations occurring during continuous locomotion, locomotion onsets and any other short movements not falling into either of these two categories, though the vast majority occurred during continuous locomotion).

For acceleration triggered averages of $\Delta F/F$, single average $\Delta F/F$ traces were derived for each field (Figs 1 and 2), putative single axon (Fig. 4), or photometry recording location (Fig. 5, Extended Data Fig. 10) across all identified accelerations (meeting acceleration criteria, triggered on the zero crossing of the acceleration trace when the acceleration was increasing and crossed a threshold value >1.7 m s^{-2}) in an imaging session; and these traces were averaged across sessions and mice to generate summary traces. $\Delta F/F$ triggered averages of acceleration were calculated analogously (Fig. 2g, Extended Data Fig. 4i, bottom, triggered on the onsets of significant, positive-going $\Delta F/F$ transients). For these traces, and for analysis of amplitudes of preceding and following accelerations bursts (Extended Data Fig. 5c, d) only significant transients <0.5 s duration were included to avoid

inclusion of any sustained summated transients. Shuffled triggered averages were computed relative to an equivalent number of randomly selected time-points (randsample in MATLAB). Correlations (Pearson's) between acceleration and $\Delta F/F$ were calculated between the (concatenated) traces around all initiation bins (± 750 ms around each) or continuous locomotion periods ($+2$ s after locomotion initiation to locomotion termination). Note that differences in the criteria for selecting different behaviour periods (locomotion initiations, terminations, continuous running periods, etc) results in the inclusion of a different number of fields or axons for each behaviour (that is, Fig. 2a–e).

Single-photon fibre photometry fluorescence data was first averaged over 35.7-ms bins and then corrected for background signal (intrinsic fluorescence and laser bleed-through). The signal recorded in the unlabelled cortex (estimated in a subset of the recordings) was assumed to be background and this signal was subtracted from the striatum signal. After this subtraction, the remaining photometry signal (assumed to be GCaMP6f fluorescence) was analysed identically to the whole field two-photon imaging data sets described above.

Relationship of acceleration to ChR2 axon stimulation. Significant effects of laser stimulation on locomotion initiations (Fig. 3d–g) were assessed by comparing the mean absolute value of acceleration within a 0.5–2-s window (for each mouse and across all mice, Fig. 3f) or for each bin (Fig. 3g) following stimulation train onsets that were delivered during rest (no large accelerations within 2 s before stimulation) across all mice and stimulation trains to the means obtained from 1,000 rounds of randomly selecting an equivalent number of non-laser stimulation rest periods from the same stimulation sessions. Sessions were included if mice exhibited spontaneous locomotion/rest transitions in the absence of stimulation and exhibited average resting bout durations of >6 s (to allow comparison with spontaneous transitions from rest to running). Stimulation effects were considered significant if the post-stimulation means were greater than 990 of the 1,000 randomly selected means ($P < 0.01$). Note that because we analysed laser train onsets that were preceded by 2 s of rest, there was a slightly higher probability for mice to be moving in a window after the stimulation onset simply by chance. This explains the apparent small change in the control group (Fig. 3f) at laser train onset and in the shuffle group (Fig. 3g). A similar test was applied to assess significant frequency dependent acceleration entrainment (Extended Data Fig. 6c, d). Laser burst triggered averages of acceleration were computed during locomotion periods beginning after laser train onset and the mean of absolute value of these triggered averages were compared with 1,000 averages from randomly selected non-laser stimulation locomotion periods. Consistent phase relationships between the laser stimulation and acceleration produce significant positive and negative peaks in the triggered average (Extended Data Fig. 6c,d), whereas traces with no consistent phase relationship result in flat triggered averages (see controls, Extended Data Fig. 6c, d). Multi-taper power spectral densities of acceleration (Fig. 3h) were constructed for all locomotion periods (minimum 3 s of locomotion per stimulation train period) during 6 Hz and 3 Hz stimulation periods in each block using the mtspectrumc function in the Chronux library (http://chronux.org/) with 5 tapers and a time bandwidth product of 3 over the interval 1 Hz to 8 Hz. Power spectra across blocks were averaged to produce mean power spectra for each mouse (one each for 6 and 3 Hz stimulations, Fig. 3h). The centre of mass (Fig. 3i–l, Extended Data Fig. 6f–h) was calculated from the top 25% of the mean power spectra for each mouse (although highly similar results were obtained using the top 50%, 75% or all of the power spectra).
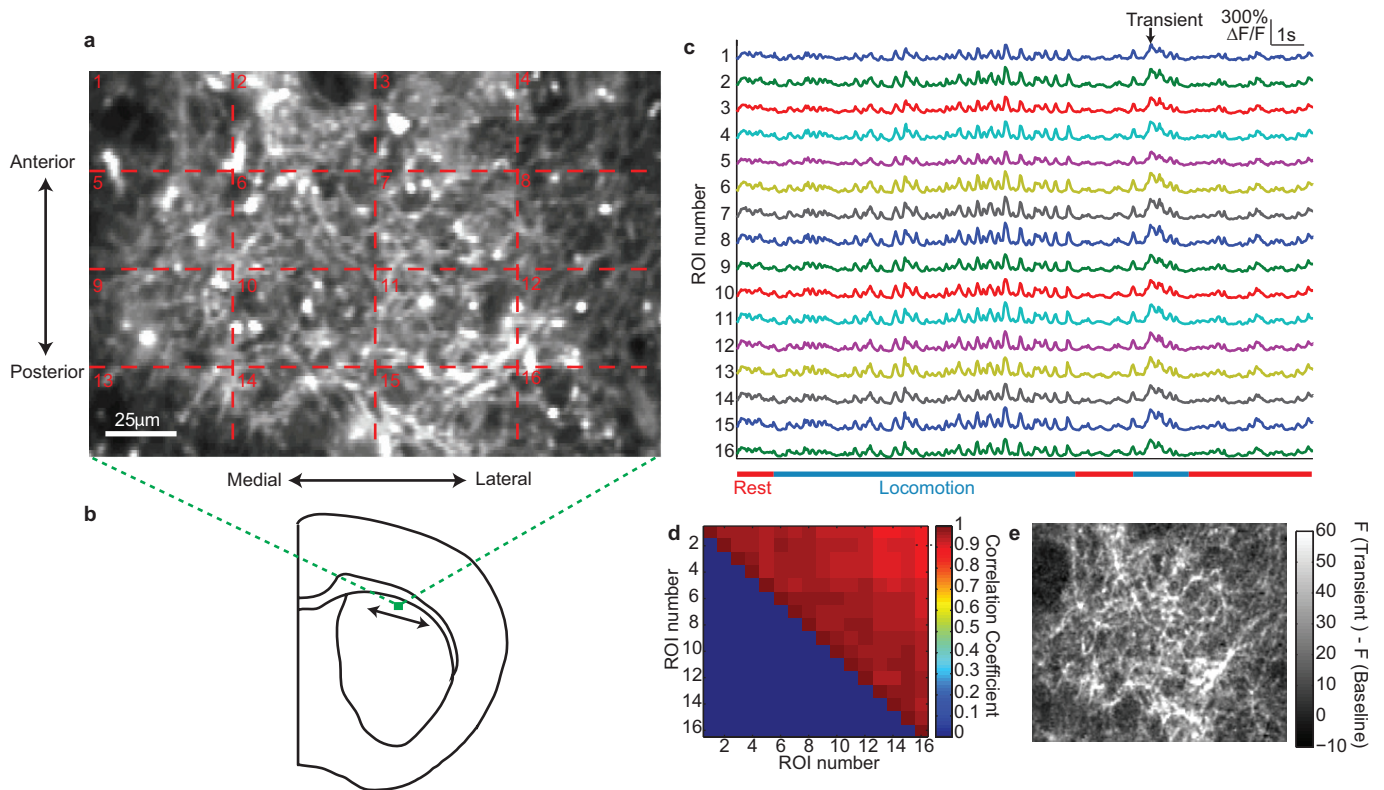
Classification of functional signalling related to reward and locomotion across putative single axons and striatum locations. Axon heterogeneity in single fields relative to reward and locomotion periods (Fig. 4a, i) was visualized by computing the mean fluorescence image during locomotion bins (see above) and subtracting the mean fluorescence image during reward delivery (a 750-ms window following reward delivery). Locomotion index (Fig. 4n and Extended Data Figs 7, 8, 10g) was the difference between the mean $\Delta F/F$ during locomotion and rest ($\Delta/\Delta F_{move} - \Delta/\Delta F_{rest}$) and axons were classified as significantly locomotion responsive via a Wilcoxon rank-sum test ($P < 0.05$) between all locomotion and rest $\Delta F/F$ values. Reward responses (Fig. 4n and Extended Data Figs 7, 8, 10g) were defined as the mean $\Delta F/F$ in a 300-ms window after reward delivery. Significance of reward responses were computed with a bootstrap test ($P < 0.05$) where the P value was the probability of receiving an equivalent or larger mean value from 1,000 rounds of randomly selecting a trigger bin from all non-reward bins.

ROC analysis. ROC (receiver operating characteristic) curves (Extended Data Fig. 4n, o) to assess the ability of calcium transients to discriminate locomotion from rest were computed using the 'perfcurve' function in MATLAB for all bins for each imaging field that were classified as locomotion or rest based on the criteria defined above. The positive state was defined as locomotion, the negative as rest (Extended Data Fig. 4n). For the onset ROC analysis to assess ability of calcium transients to discriminate pre-locomotor from other rest periods (Extended Data Fig. 4o), all resting bins were classified as either being pre-onset (positive state, within 250 ms before defined onset; see above) or non-pre onset (negative state).

Histology. Mice with injections targeting SNc or VTA (see above) were perfused trans-cardially with 15ml PBS (Fischer) and 15 ml of 4% paraformaldehyde (EMS). Brains were stored in PBS at 4 °C then transferred to 40% sucrose (Fischer) overnight before sectioning. Coronal slices (40–50 μm) were cut on a freezing microtome and stored at 4 °C in PBS. For immunostaining of dopaminergic neurons, sections from a subset of mice were blocked in 5% serum, incubated overnight at 4 °C with antibodies for tyrosine hydroxylase (1:700 dilution, Millipore AB152, Fig. 1d, Extended Data Fig. 7), then incubated with secondary antibodies tagged with Alexa Fluor 594 (Jackson). Large area imaging of tyrosine hydroxylase and GCaMP6f expression was performed on an Olympus Slide Scanner (VS120) microscope, and high magnification imaging of co-labelling (Fig. 1d, right) was performed with a confocal microscope.

51. Harvey, C. D., Collman, F., Dombeck, D. A. & Tank, D. W. Intracellular dynamics of hippocampal place cells during virtual navigation. *Nature* **461,** 941–946 (2009).
52. Heys, J. G., Rangarajan, K. V. & Dombeck, D. A. The functional micro-organization of grid cells revealed by cellular-resolution imaging. *Neuron* **84,** 1079–1090 (2014).
53. Sheffield, M. E. & Dombeck, D. A. Calcium transient prevalence across the dendritic arbour predicts place field properties. *Nature* **517,** 200–204 (2015).
54. Hofer, S. B. *et al.* Differential connectivity and response dynamics of excitatory and inhibitory neurons in visual cortex. *Nat. Neurosci.* **14,** 1045–1052 (2011).
55. Miyashita, T., Shao, Y. R., Chung, J., Pourzia, O. & Feldman, D. E. Long-term channelrhodopsin-2 (ChR2) expression can induce abnormal axonal morphology and targeting in cerebral cortex. *Front. Neural Circuits* **7,** 8 (2013).
56. Miri, A. *et al.* Spatial gradients and multidimensional dynamics in a neural integrator circuit. *Nat. Neurosci.* **14,** 1150–1159 (2011).
57. Mukamel, E. A., Nimmerjahn, A. & Schnitzer, M. J. Automated analysis of cellular signals from large-scale calcium imaging data. *Neuron* **63,** 747–760 (2009).

a

Anterior

Posterior

25µm

Medial ⟵ ⟶ Lateral

b

c

Transient   300% ΔF/F ⌐1s

ROI number

Rest   Locomotion

d

ROI number

Correlation Coefficient

ROI number

e

F (Transient) - F (Baseline)

Extended Data Figure 1 | Synchronized dopamine projection axon dynamics across a single field in dorsal striatum. a, Representative mean fluorescence image in dorsal striatum of a dense field of dopamine axons (compare to the sparse fields from sparse labelling in Fig. 4c, i) from one mouse (out of six) labelled with GCaMP6f. **b,** Coronal schematic showing approximate location and scale of region imaged at top. Arrow indicates the approximate range of medial/lateral positions used for two-photon imaging (see Methods). **c,** ΔF/F traces for the rectangular ROIs indicated in **a**. **d,** Correlation matrix for the ROIs indicated in **a**. Note high degree of transient co-activation across ROIs. **e,** Mean image of fluorescence during the transient indicated by the arrow in **c** minus mean image of fluorescence during non-transient periods for the field shown in **a**. Note that the morphology of active regions closely resembles the morphology of GCaMP6f-expressing axons in the whole field in **a**, indicating synchronous activation of large, dense regions of axons, likely belonging to several different parent neurons.
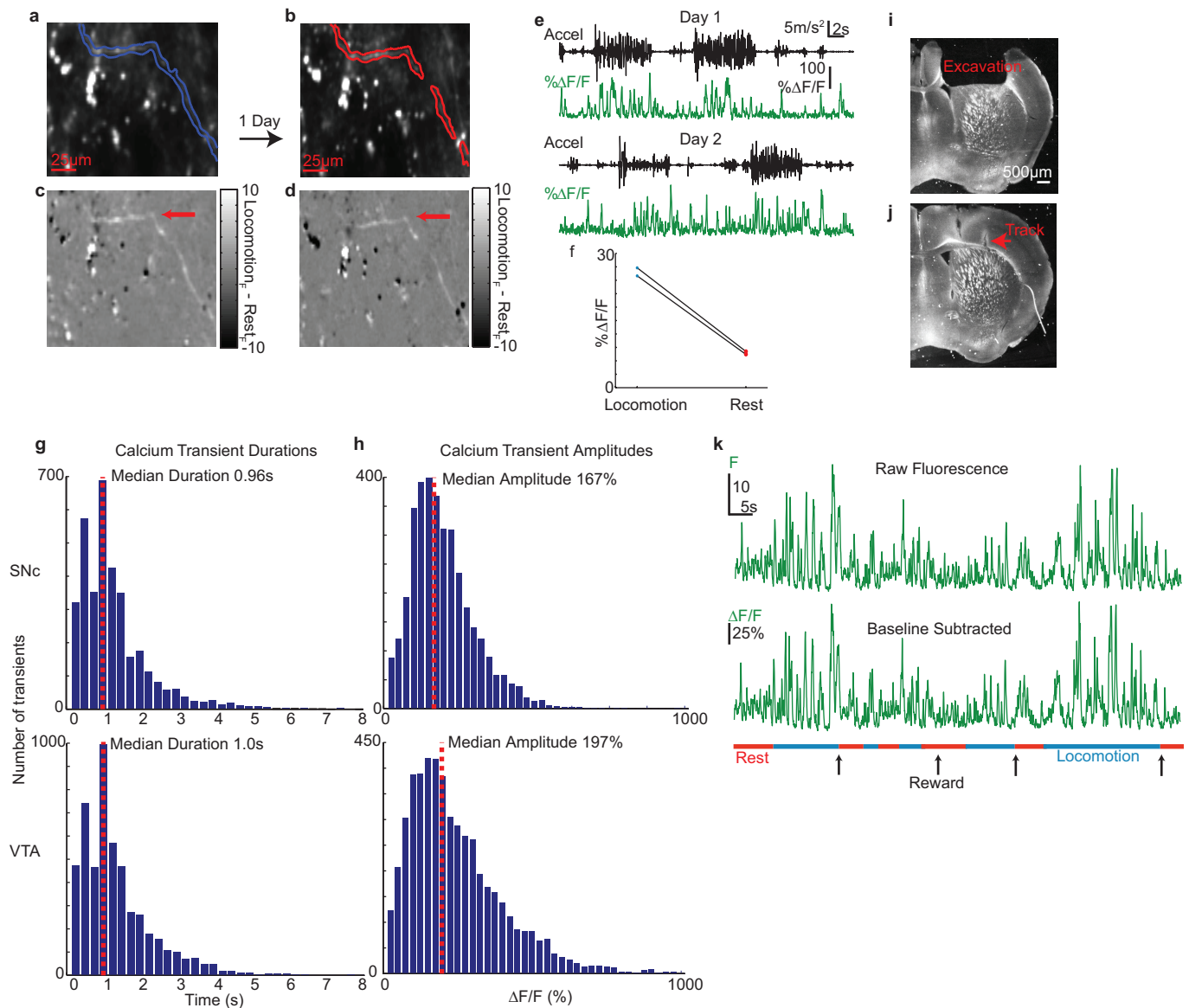
Extended Data Figure 2 | Further characterization of two-photon imaging and analysis methods. a, b, Top, example mean fluorescence images of a putative single SNc axon imaged over 2 consecutive days in one mouse. **c, d,** Mean images of fluorescence during locomotion periods minus mean image of fluorescence during reward periods for fields in **a** and **b**. White axonal regions indicate regions of elevated signalling during locomotion. Note the similar morphology and behaviour signalling of the identified axon (red arrow) over days. **e,** Acceleration (black) and $\Delta F/F$ (green) for the identified axon in **a–d** across the two imaging days. Note the similar transient amplitudes and the elevated transient signalling during locomotion acceleration periods. **f,** Mean transient $\Delta F/F$ (mean of significant transients, excluding baseline periods) during locomotion and rest on days 1 and 2 for the axon shown in **a–d**. **g,** Histograms of calcium transient duration times across all putative single axons imaged in dorsal striatum from SNc ($n = 3{,}556$ transients, 5 mice top) and VTA

($n = 5140$ transients, 5 mice bottom). Note the similar duration profile across the two populations (medians not significantly different, $P > 0.05$ Wilcoxon sign-rank test). **h,** Histograms of maximum calcium transient amplitudes across all putative single axons imaged in dorsal striatum from SNc (top) and VTA (bottom) (medians not significantly different, $P > 0.05$ Wilcoxon sign-rank test). **i,** Post-mortem image of a coronal section from a representative mouse showing the striatum imaging cannula window cortical lesion site. **j,** Post-mortem image from a different mouse than **i** that was used for fibre photometry recording (fibre track indicated by arrow). **k,** Similarity of raw (no baseline normalization) whole-field GCaMP6f F trace (top) with baseline normalized $\Delta F/F$ trace (bottom) for the example whole-field imaging session shown in Fig. 1e. In the top trace, note the lack of baseline change over the recording session and particularly the stability of the baseline level during locomotion periods. Bottom trace is duplicate of trace in Fig. 1e.
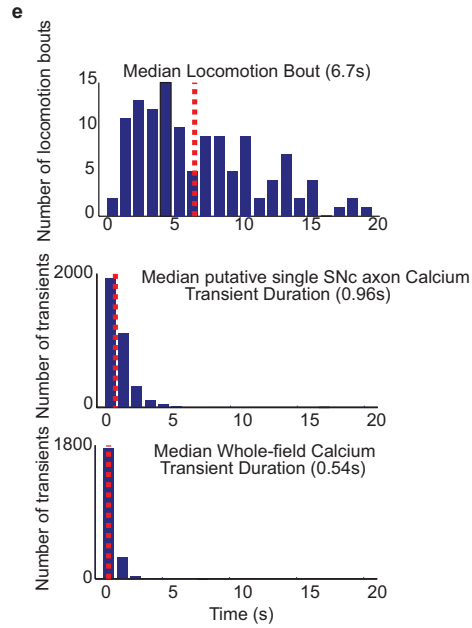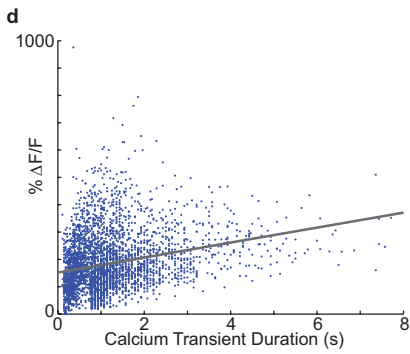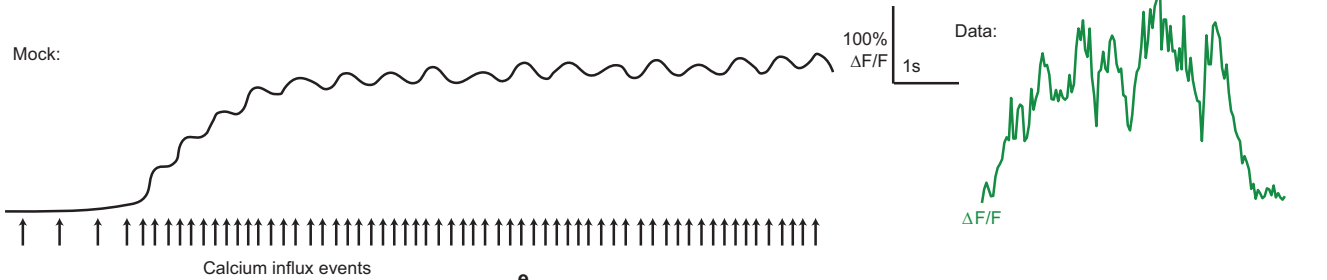
a Calcium transient due to a short ms timescale influx of calcium

Mock:

75% ΔF/F 200ms

Data:

ΔF/F

Calcium influx events
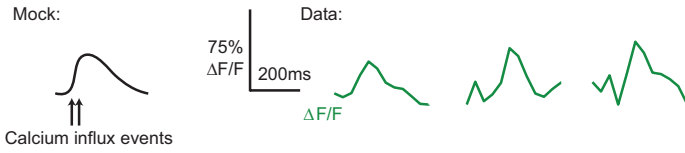
b Calcium transients due to multiple influx events separated by less than indicator decay time

Mock:

75% ΔF/F 200ms

Data:

ΔF/F

Calcium influx events
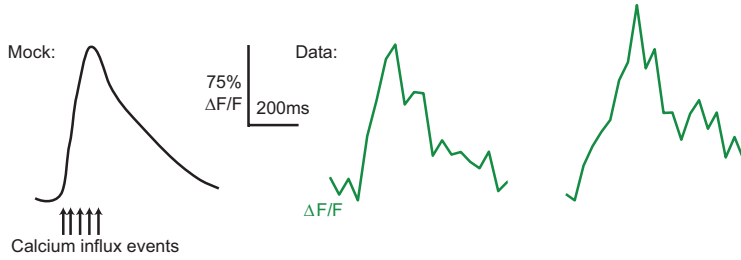
c Calcium transients due to sustained increase in the rate of influx events separated by less than the indicator decay time

One of longest transient increases (~4.8s). Note that sustained shifts as show at left were not observed.

Mock:

100% ΔF/F 1s

Data:

ΔF/F

Calcium influx events

d

%ΔF/F

Calcium Transient Duration (s)

e

Number of locomotion bouts

Median Locomotion Bout (6.7s)

Number of transients

Median putative single SNc axon Calcium Transient Duration (0.96s)

Number of transients

Median Whole-field Calcium Transient Duration (0.54s)

Time (s)

Extended Data Figure 3 | See next page for caption.

Extended Data Figure 3 | Interpretation of mechanisms underlying calcium transients and characterization of putative single dopamine axon calcium transients. a, Left, mock trace representing expected GCaMP6f calcium transient from a short millisecond timescale influx of calcium (arrows; for example, short burst of action potentials over tens of milliseconds; local modulation may also contribute to calcium influx). Right, three representative low-amplitude, short duration calcium transients (from putative single dopamine axons in dorsal striatum) (see Methods, Fig. 4) that display onset and decay kinetics consistent with mock transient (left). **b**, Left, mock trace representing expected GCaMP6f calcium transient from multiple calcium influx events separated by less than the indicator decay time (arrows; for example, longer burst of action potential firing over ~100s of milliseconds). Right, representative larger amplitude calcium transients (from putative single dopamine axons in dorsal striatum) with rapid rise times consistent with mock transient (left). **c**, Left, mock trace representing expected GCaMP6f calcium transient from a sustained increase in the rate of influx events separated by less than the decay time (for example, sustained increase in action potential firing). Right, representative trace of one of the longest duration calcium transients observed (from putative single dopamine axon in dorsal striatum). Note that no sustained increases (baseline shifts) similar to the mock trace (left) were observed in single axon recordings or whole-field

$\Delta F/F$ measurements; however, the long duration transient shown (right) indicates that if such sustained increases had occurred, they would have been detected using our methods. Also, note that the mock traces shown in **a**–**c** are for descriptive purposes and are not based on new data. These traces are based on two main assumptions: (1) $\Delta F/F$ is a monotonically increasing function of intracellular calcium concentration, which itself is a monotonically increasing function of the number of underlying action potentials (that is, a greater number of action potentials leads to a larger $\Delta F/F$, but the relationship is not necessarily linear); and (2) $\Delta F/F$ transients summate (not necessarily linearly) when they overlap in time. **d**, Duration versus peak $\Delta F/F$ for all identified significant calcium transients in putative single SNc originating axons (see Methods, Fig. 4, $n = 3,556$ transients from 73 axons in 5 mice; Spearman's Rho $= 0.3$ $P < 10^{-10}$). **e**, Histogram of sustained locomotion period durations (from SNc injected mice, $n = 5$, top) and calcium transient durations for all putative single SNc axons ($n = 5$ mice, mid) and all whole-fields ($n = 6$ mice, bottom). Note that the median calcium transient duration (for either single axon or whole-field) is far less than the median locomotion duration, indicating that the increase in dopamine axon GCaMP6f $\Delta F/F$ observed during locomotion is due to an increase in relatively short duration calcium transients, rather than long-duration (sustained) increases in $\Delta F/F$.
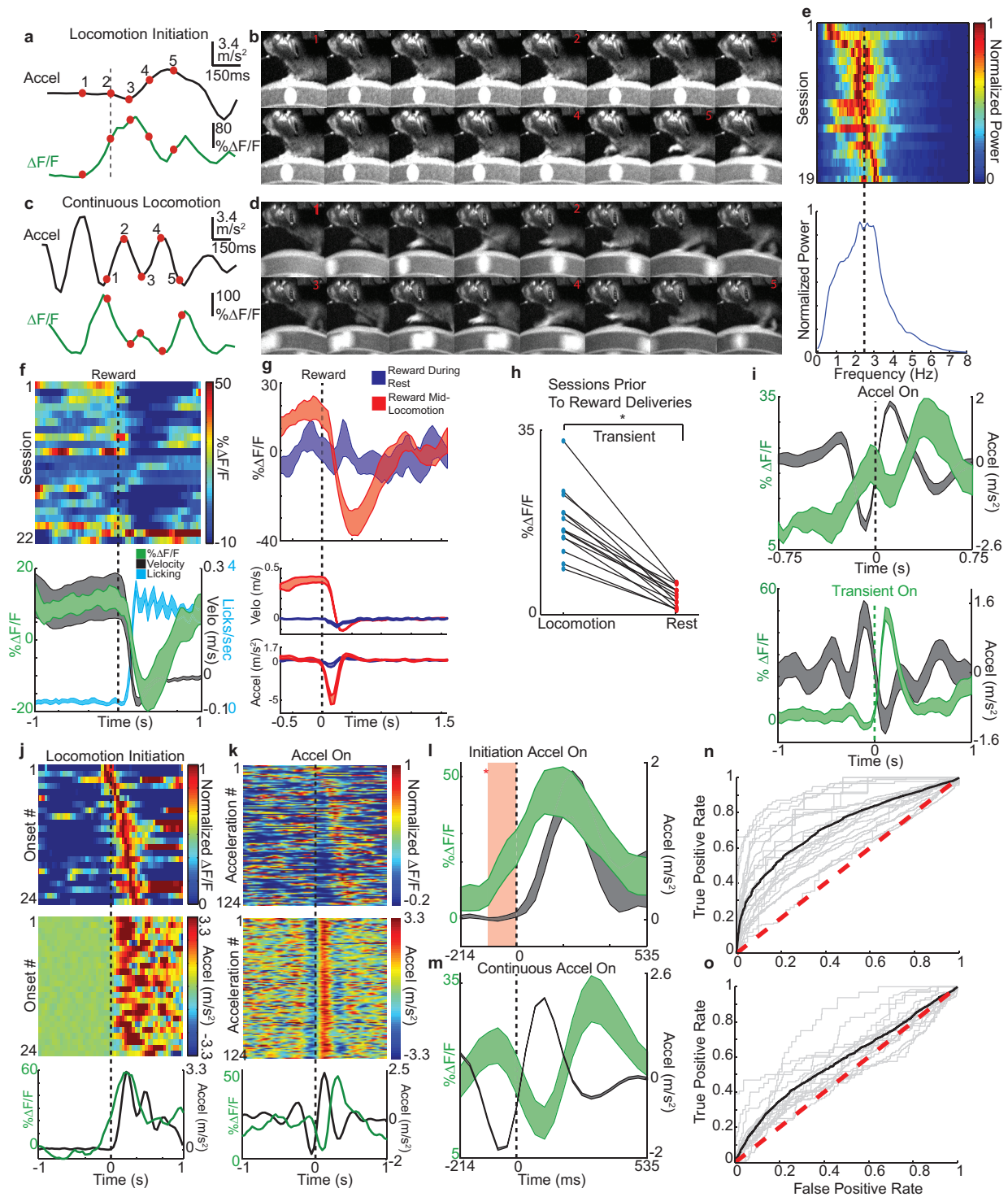
Extended Data Figure 4 | See next page for caption.

Extended Data Figure 4 | Further characterization of acceleration-associated dopamine signalling. a, Representative whole-field $\Delta F/F$ fluorescence trace (one field from one out of six mice, green) aligned to treadmill acceleration (black) during a locomotion onset (dashed line: onset). **b**, Video frames of mouse for time points shown in **a**. **c, d**, Same as **a** and **b** but for a period of continuous locomotion. **e**, Top, normalized spectral power of treadmill acceleration trace during continuous locomotion periods for each two-photon imaging session (each row represents a session, $n = 6$ mice). Bottom, normalized mean power from all sessions shown in **e**, top. **f**, Top, mean whole-field $\Delta F/F$ trace triggered on reward delivery time for all fields; each row is mean for each field/session ($n = 22$ fields, 6 mice). Bottom, mean treadmill velocity (black), mean whole-field $\Delta F/F$ (green), and spout licking (light blue) all triggered on reward time (mean across all 22 fields/sessions in 6 mice). **g**, Mean whole-field $\Delta F/F$ (top), velocity (mid), and acceleration (bottom) for trials in which reward was delivered mid-locomotion ($n = 13$ sessions, 4 mice, red) or when animals were at rest ($n = 12$ sessions, 4 mice, blue). Note the sharp decrease in $\Delta F/F$ relative to baseline when animals decelerated from locomotion to consume the reward and the relative absence of phasic reward signalling when animals were given reward from rest. Reward responses were also not observed in single SNc axons when animals received reward from rest (see Extended Data Fig. 9). **h**, Comparison of mean whole-field fluorescence change from significant calcium transients (excluding baseline periods) between locomotion and resting periods; each point represents mean $\Delta F/F$ for running or resting over one session for each field (lines connect same field/session). All fields included here were imaged before mice ever receiving any rewards on the treadmill ($n = 14$ fields, 4 mice). $*P < 10^{-5}$ (Wilcoxon rank-sum test). **i**, top, Mean acceleration (black) and whole-field $\Delta F/F$ (green) triggered on acceleration onsets (mean across all fields) during

continuous locomotion. Bottom, mean acceleration (black) triggered on all short duration calcium transients (green, mean of transients) during continuous locomotion across all fields. All fields included here were imaged before mice ever receiving any rewards on the treadmill ($n = 14$ fields, 4 mice). **j**, Top, whole-field $\Delta F/F$ from all locomotion initiations in a representative single session (single imaging field, single session, one out of 6 mice); each row represents a single locomotion initiation time period (sorted by peak $\Delta F/F$ time). Mid, treadmill accelerations corresponding to locomotion initiations shown in **j**, top. Bottom, average of acceleration (black) and $\Delta F/F$ (green) across all locomotion onset traces displayed in Top and Mid panels. **k**, same as **j**, but for continuous locomotion periods. **l**, Reproduction of Fig. 2a with zoomed-in time axes to show the timing of the mean DF/F in relation to the first acceleration at locomotion initiations from rest. Shaded red region indicates bins that were significantly ($*P < 0.01$, Wilcoxon sign-rank, $n = 15$ fields in 6 mice) elevated relative to rest baseline. Shaded region covers ~107 ms before acceleration onset. **m**, Reproduction of Fig. 2b with zoomed-in time axes to show the timing of the mean dopamine transient in relation to the accelerations during continuous locomotion ($n = 18$ fields, 6 mice). **n**, ROC curves for each two-photon whole-field $\Delta F/F$ trace ($n = 22$ fields from 6 mice, grey; mean, black line) assessed for ability to discriminate locomotion versus resting periods (21 out of 22 exhibited significant discriminability, $P < 0.01$). Area under the curve (AUC) $= 0.76 \pm 0.02$ (mean $\pm$ s.e.m.). **o**, ROC curves for each two-photon whole-field $\Delta F/F$ trace ($n = 17$ fields in 6 mice, grey; mean, black line) assessed for ability to discriminate pre-locomotion onset rest periods (250 ms before onset) from other rest periods (10 out of 17 exhibited significant discriminability, $P < 0.01$, two sessions included did not meet onset criteria for Fig. 2a, Methods). AUC $= 0.58 \pm 0.02$ (mean $\pm$ s.e.m.). Dashed red lines indicate the line of no discrimination. Shaded regions in **f, g, i, l, m** denotes mean $\pm$ s.e.m.
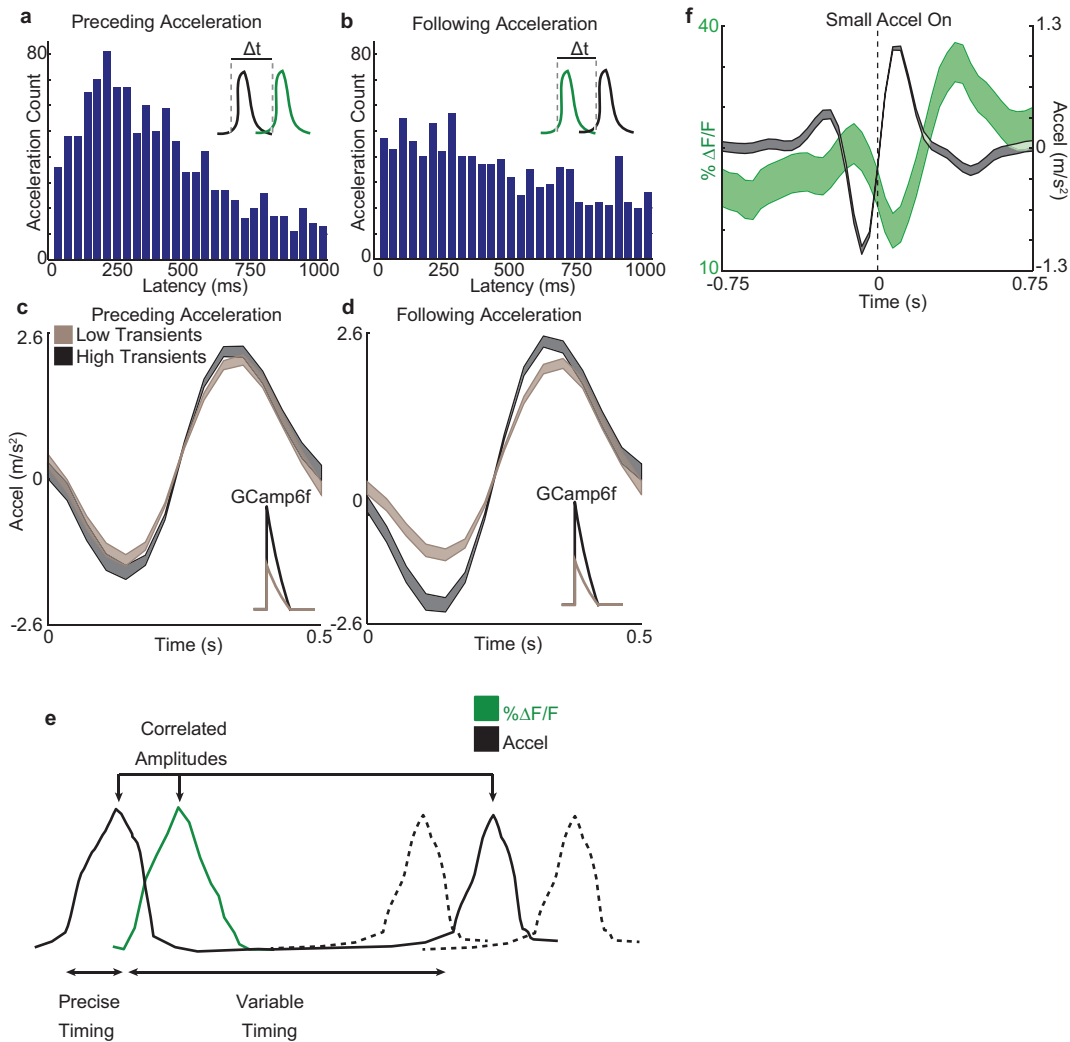
Extended Data Figure 5 | Dopamine axon calcium transients are temporally associated with preceding acceleration bursts and their amplitude is correlated with both preceding and subsequent acceleration bursts. a, **b**, Distribution of latencies from each significant calcium transient onset (mean whole-field fluorescence; 6 mice) to the first acceleration burst onset within 1 s preceding ($n = 1,087$, 6 mice, **a**) or following ($n = 990$, 6 mice, **b**) during continuous locomotion. Latencies are less variable (F-test for difference between variance of latencies, $P = 7.1 \times 10^{-5}$) and shorter (Wilcoxon test for difference between latency means, $P = 1.2 \times 10^{-5}$) to the preceding acceleration onsets, indicating more precise relative timing between the GCamp6f transients and the preceding acceleration burst versus the following acceleration burst. **c**, **d**, Mean acceleration traces from the first acceleration (within 1 s) preceding (**c**) or following (**d**) all short duration (<0.5 s) large amplitude (>75th percentile, $n = 149$ transients, grey) and small amplitude (<25th percentile, $n = 149$ transients, bronze) calcium transients occurring during continuous locomotion; aligned on acceleration onsets.

Insets are schematics of the GCaMP6f transients. A significant correlation is present between the transient amplitudes and the immediately preceding acceleration amplitudes (Spearman's Rho = 0.16, $P = 1.2 \times 10^{-4}$, from all transient-acceleration pairs; binned data from this plot shown in **c**). A significant correlation is also present between the transient amplitudes and the immediately following acceleration amplitudes (Spearman's Rho = 0.13, $P = 0.006$, from all transient-acceleration pairs; binned data from this plot shown in **d**). **e**, Schematic summarizing relationship between the timing and amplitude of dopamine axon calcium transients and acceleration bursts during continuous locomotion. **f**, Mean acceleration (black) and whole-field $\Delta F/F$ (green) all triggered on all accelerations during continuous locomotion that were less than 1.7 m s^{-2} in amplitude ($n = 596$ accelerations, $n = 6$ mice); this demonstrates that dopamine axon GCaMP6f signalling displays a timing preference with respect to small amplitude accelerations, with similar timing and amplitude to that shown in Fig. 2b (which includes both large and small amplitude accelerations).
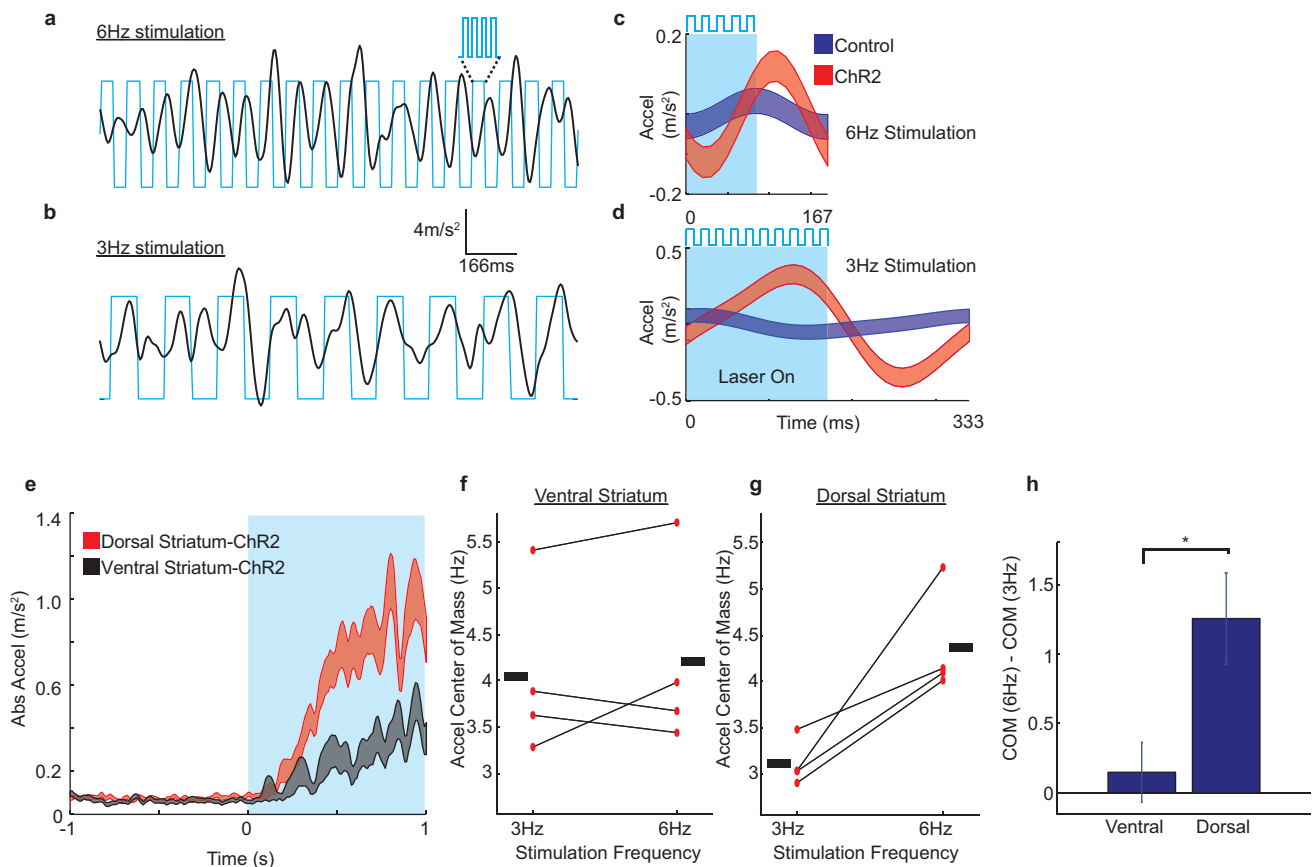
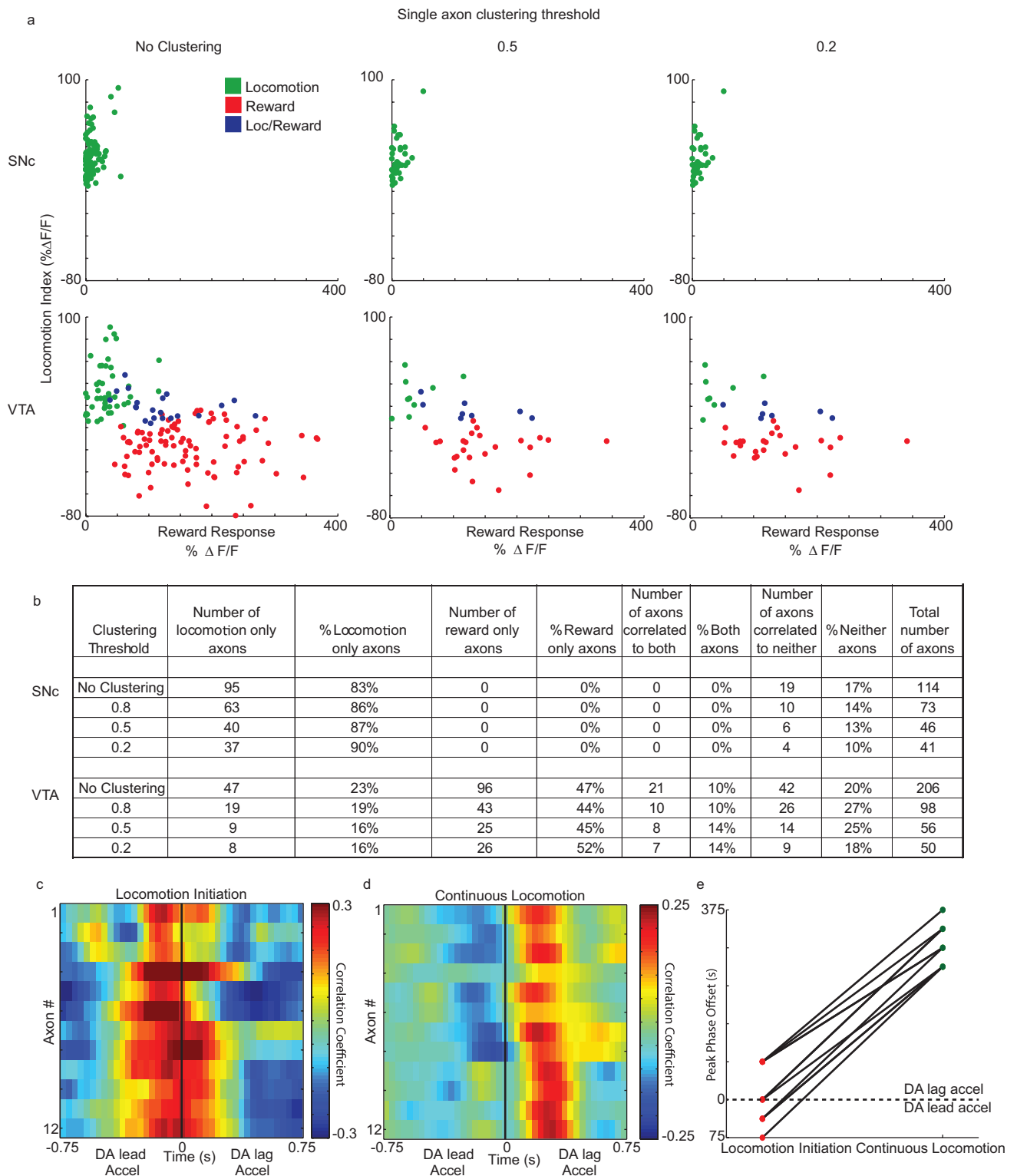**Extended Data Figure 6 | Pulsed optogenetic stimulation of dorsal-striatum-projecting and ventral-striatum-projecting dopamine axons.** **a–d**, Pulsed optogenetic stimulation of dorsal-striatum-projecting dopamine axons can entrain accelerations during locomotion. **e–h**, Pulsed optogenetic stimulation of ventral-striatum-projecting dopamine axons leads to little effect on locomotion. **a**, **b**, Representative acceleration traces from continuous locomotion periods during (and initiated by) 6 Hz (**a**) and 3 Hz (**b**) laser stimulation trains in the same mouse. Blue, laser stimulation train, one mouse out of seven. **c**, **d**, Mean accelerations triggered on individual laser burst onsets during continuous locomotion periods for 6 Hz (**c**) and 3 Hz (**d**) across all laser bursts in all mice and sessions ($n = 7$ mice). **e**, Mean absolute value of mouse accelerations aligned on onset of laser stimulation train applied to mice at rest (mean across all stimulation onsets, $n = 55$ and 91 for ventral and dorsal respectively, in all sessions and mice, 3 and 6 Hz stimulation included). Dorsal and ventral striatum stimulations are from same ChR2-expressing mice ($n = 4$). Three mice were not stimulated in ventral striatum and

thus not included in this figure. Mean acceleration elicited by ventral stimulation was significantly ($P < 0.01$, Wilcoxon rank-sum test) less than that elicited by dorsal axon stimulation. However, acceleration from ventral stimulation was significantly greater than chance ($P < 0.01$ shuffle test). This small effect in the ventral striatum could be due to activation of fibres, which also project to the dorsal striatum or to an increase in arousal. Although note that acceleration frequency during locomotion was not altered for stimulation in ventral striatum (see **f**, **h**). **f**, **g**, Centre of mass of acceleration power spectra for each mouse for locomotion periods initiated during 3 or 6 Hz stimulations ($n = 4$ mice). Horizontal bars indicate means, lines connect same mouse. **h**, Mean difference between the centre of mass of the acceleration power spectra computed for locomotion periods initiated during 3 Hz or 6 Hz axon stimulations in ventral (**f**) or dorsal (**g**) striatum. Positive values indicate a shift towards higher frequency accelerations for 6 Hz stimulations. *$P < 0.05$, Wilcoxon rank-sum test.
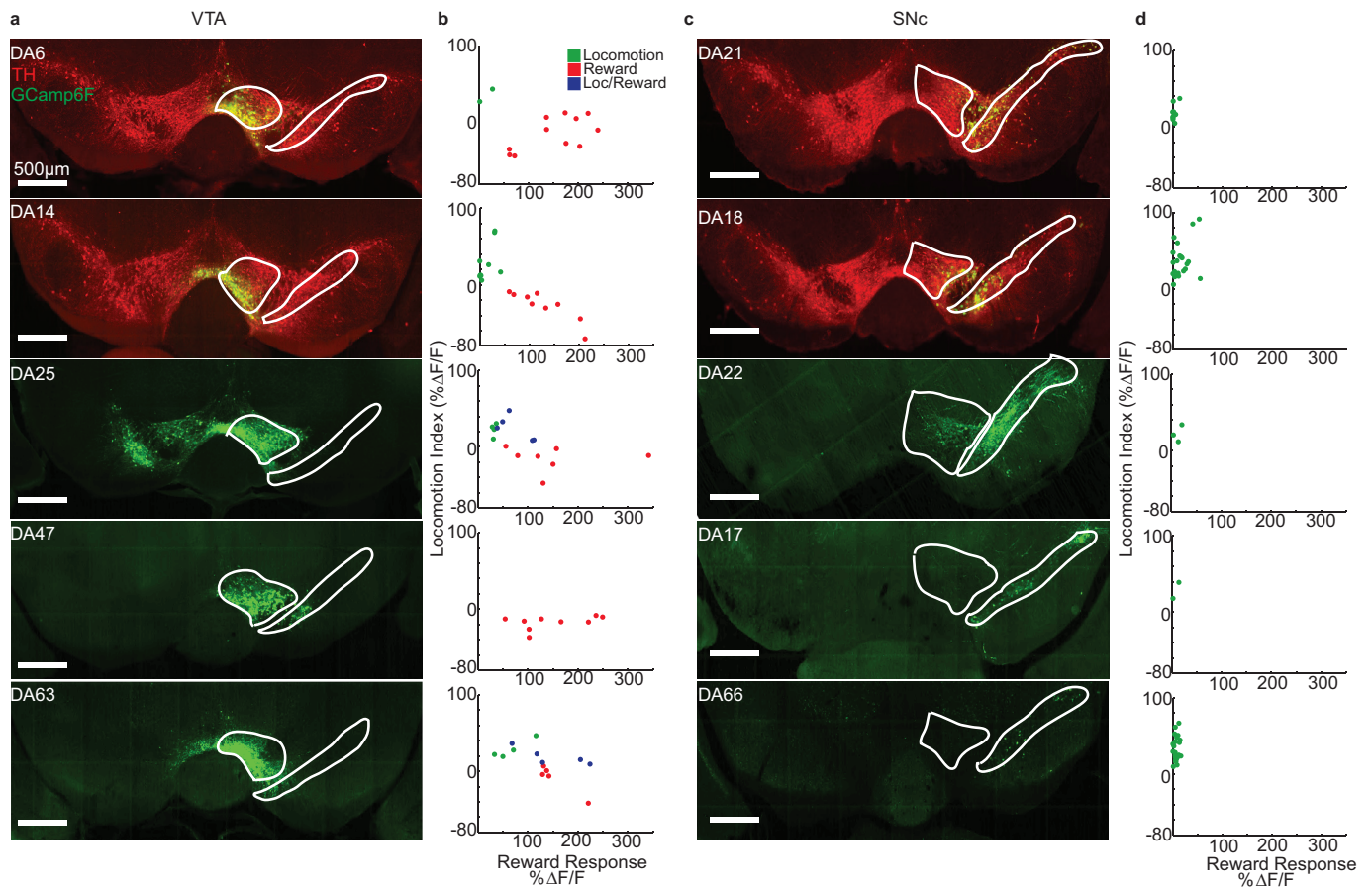
Extended Data Figure 7 | Histology and response distributions from each sparsely injected mouse. a, GCaMP6f expression (green) and immunofluorescence (red) from all VTA-targeted mice ($n = 5$). **b**, Reward response versus locomotion index (as in Fig. 4n) for each axon recorded from the corresponding mice in **a**. Green, significant locomotion; red, significant reward; blue both significant; neither significant not shown. **c**, **d**, Same as **a** and **b**, except from all SNc-injected mice ($n = 5$). Six out of ten mice were not stained for tyrosine hydroxylase. Scale bars, 500 μm.

a Single axon clustering threshold

b

|	Clustering Threshold	Number of locomotion only axons	%Locomotion only axons	Number of reward only axons	%Reward only axons	Number of axons correlated to both	%Both axons	Number of axons correlated to neither	%Neither axons	Total number of axons
SNc	No Clustering	95	83%	0	0%	0	0%	19	17%	114
	0.8	63	86%	0	0%	0	0%	10	14%	73
	0.5	40	87%	0	0%	0	0%	6	13%	46
	0.2	37	90%	0	0%	0	0%	4	10%	41
VTA	No Clustering	47	23%	96	47%	21	10%	42	20%	206
	0.8	19	19%	43	44%	10	10%	26	27%	98
	0.5	9	16%	25	45%	8	14%	14	25%	56
	0.2	8	16%	26	52%	7	14%	9	18%	50

Extended Data Figure 8 | Distribution of reward and locomotion indexes and fraction of reward and locomotion signalling axons from VTA and SNc are highly similar using different correlation thresholds for clustering axon segments (a, b); single axon signaling timing during locomotion onset versus continuous locomotion (c–e). a, Reward response versus locomotion index for putative single axons from SNc ($n = 5$ mice, top row) and VTA ($n = 5$ mice, bottom row) using different correlation thresholds (no clustering, 0.5, and 0.2) for hierarchical clustering of activity patterns (see Methods). Axons are colour-coded by significant responses to locomotion (green), reward (red), or both (blue). Note that despite the total number of putative axons decreasing with correlation threshold, the inverse relationship between locomotion and reward signalling across the population remains the same. **b**, Table showing the total numbers and fractions of responsive axons across the VTA and SNc populations for different clustering thresholds. Note that despite the total number of putative axons decreasing with correlation threshold, the fraction of axons signalling either reward, locomotion, both or neither is highly similar. **c**, Correlations (Pearson's) between acceleration and selected putative single SNc axon $\Delta F/F$ traces at different relative time-lags (that is, cross-correlations) during locomotion initiation periods; each row is mean for each axon for a single session (axons from $n = 3$ out of 5 mice). **d**, Same as **c**, but during continuous locomotion periods; same axons during same sessions as in **c**. **e**, Peak cross-correlation times for data shown in **c** and **d** (lines connect same axons during same sessions).
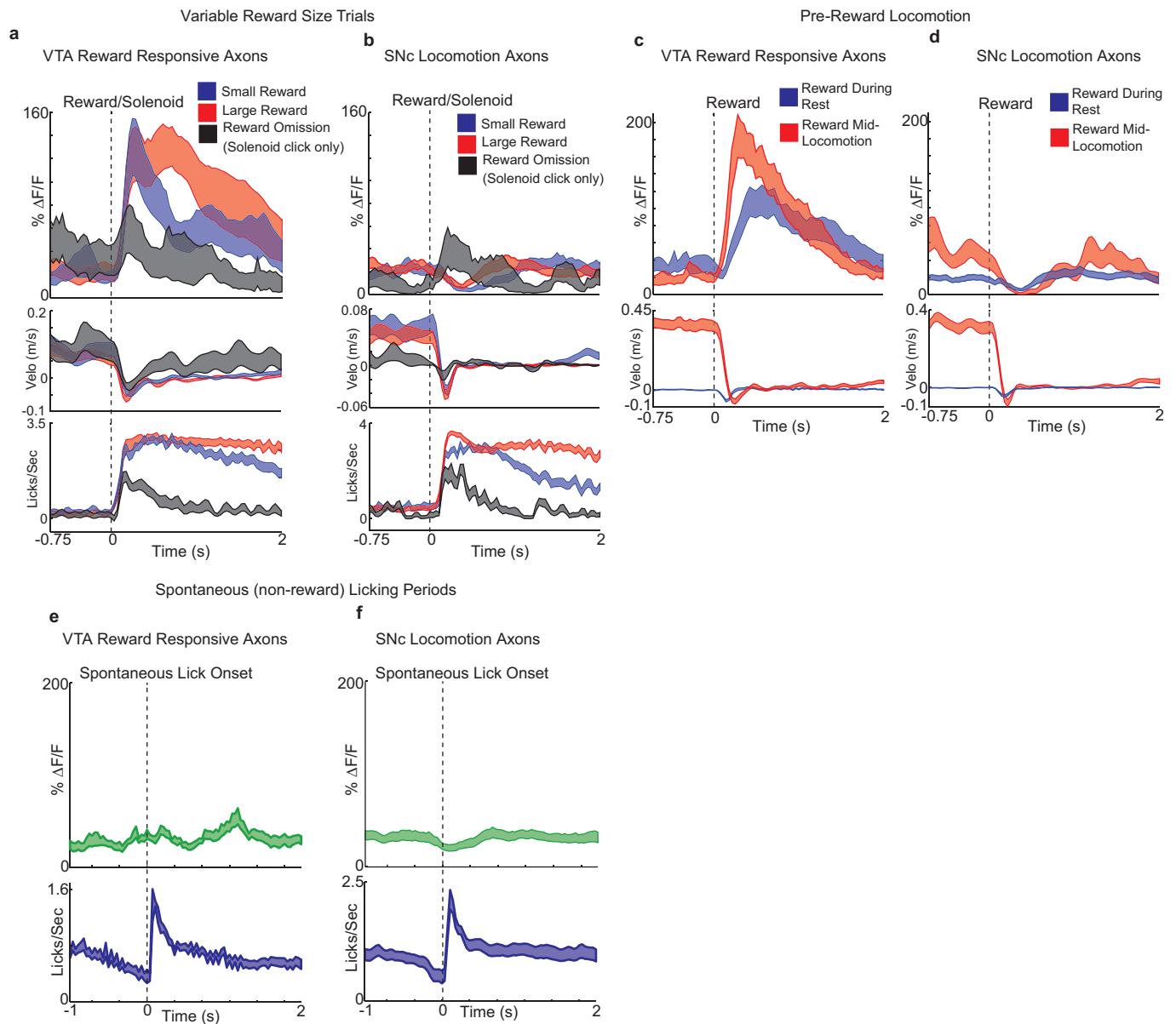
Extended Data Figure 9 | Further characterization of putative single dopamine axons in relation to reward and licking. a, Mean $\Delta F/F$ trace for VTA reward responsive axons (Methods, $n = 23$ axons, $n = 4$ mice with variable reward sessions) (top), velocity (mid), and licking (bottom) triggered on large volume (red), small volume (blue) and omission (black, solenoid click was present, but no reward delivered; Methods, $n = 17$ axons, 3 mice with omission sessions) reward deliveries. **b**, Same as **a** except for SNc locomotion responsive axons ($n = 62$ and 18 axons for reward and omission traces respectively). **c**, Mean VTA reward axon

$\Delta F/F$ trace (top) and velocity (bottom) triggered on reward deliveries during continuous locomotion (red, $n = 25$ axons) or rest periods (blue, $n = 37$ axons). **d**, Same as **c** except for SNc locomotion responsive axons ($n = 25$ and 62 axons for locomotion and rest respectively). **e**, Mean VTA reward axon $\Delta F/F$ (top) and mouse licking (bottom) triggered on spontaneous, non-reward licking onsets ($n = 15$ axons, 3 mice). **f**, Same as **e** except for SNc locomotion responsive axons ($n = 15$ axons, 3 mice). Mice that did not lick outside reward periods were excluded. Shaded regions in **a**–**f** denote mean $\pm$ s.e.m.
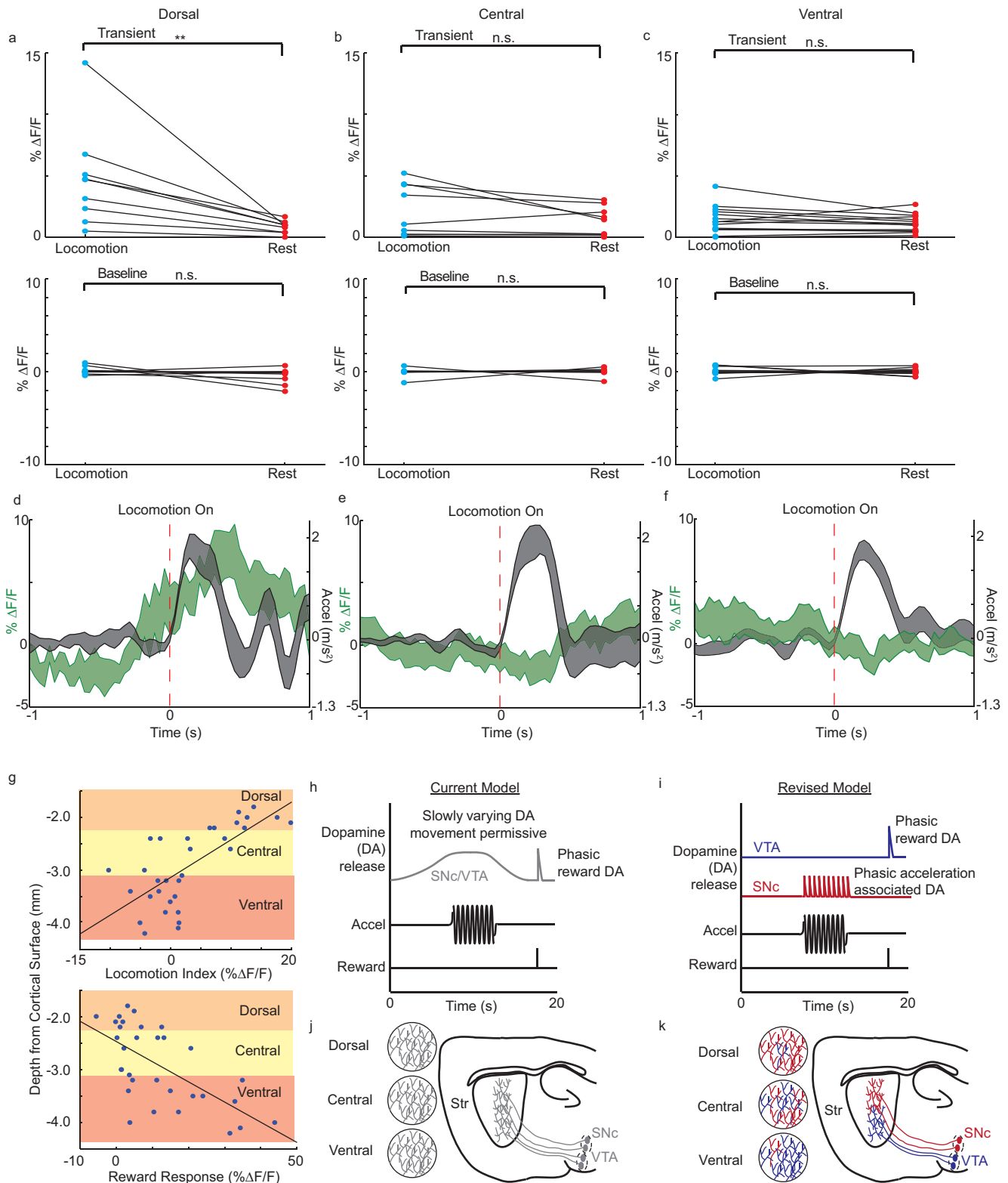
Extended Data Figure 10 | See next page for caption.

Extended Data Figure 10 | Dopamine axon locomotion signalling measured by fibre photometry from different striatal sub-regions.
a, Top, comparison of mean photometry fluorescence $\Delta F/F$ (mean of significant transients, excluding baseline periods) recorded from dorsal striatum between locomotion and resting periods; each point represents mean $\Delta F/F$ for running or resting over one session for recording from a single dorsal striatum location (lines connect same recording location/session; $n = 5$ mice). Bottom, comparison of mean baseline (periods with no significant calcium transients) photometry $\Delta F/F$ recorded from dorsal striatum between locomotion and resting periods; each point represents mean baseline $\Delta F/F$ for running or resting over one session for recording from a single dorsal striatum location (lines connect same recording location/session, $n = 5$ mice). **b**, **c**, Same as **a**, except for recordings from central and ventral striatum, respectively. **d**, Mean photometry $\Delta F/F$ recorded from dorsal striatum triggered on locomotion initiations (mean across all initiations, $n = 5$ mice). **e**, **f**, Same as **d**, except for recordings from central and ventral striatum, respectively. **g**, Locomotion index (top) and reward response (bottom) versus striatum recording depth (from data presented in Fig. 5). **h**, Schematic of prominent current model for dopamine signalling dynamics in the striatum. **i**, Schematic of our new model for dopamine signalling dynamics based on data presented here. **j**, **k**, Saggital schematics illustrating current homogenous dopamine signalling model (**j**) and our new model incorporating functional heterogeneity (**k**). **$P < 0.01$, Wilcoxon rank-sum test; n.s., not significant. Shaded regions in **d**–**f**, mean ± s.e.m across initiations ($n = 20$, 28 and 56 from dorsal, central and ventral respectively in 5 mice).